Weakly-nonlinear Holmboe waves

Joshua Cudby and Adrien Lefauve*

Department of Applied Mathematics and Theoretical Physics, University of Cambridge.
Centre for Mathematical Sciences, Wilberforce Road, Cambridge CB3 0WA, UK

Abstract

Holmboe waves are long-lived traveling waves commonly found in environmental stratified shear flows in which a relatively sharp, stable density interface is embedded within a more diffuse shear layer. Although previous research has focused on their linear properties (the Holmboe instability), and on their turbulent properties (Holmboe wave turbulence), little is known about their finite-amplitude properties in the nonlinear but non-turbulent regime. In this paper we tackle this problem with a weakly-nonlinear temporal stability analysis of Holmboe waves. We employ the rigorous and versatile amplitude expansion method recently proposed by Pham & Suslov (*R. Soc. Open Sci.* **5**: 180746, 2018), which remains well-posed a finite distance away from the critical point of linear instability. Starting with the most amplified linear Fourier mode (order 1 in amplitude), we systematically derive the hierarchy of nonlinear modes (order 2 and 3) required to obtain Landau coefficients that allow the instability to eventually saturate to a stable equilibrium amplitude. We introduce the algorithm step by step, first on a single-mode instability (suited to the weakly-stratified Kelvin-Helmholtz instability), before extending it to the more subtle case of a double-mode instability (suited to the more strongly-stratified Holmboe instability of interest). We present numerical solutions for the canonical stratified shear layer with hyperbolic-tangent symmetric profiles, shear-to-density thickness ratio $R = 5$, and Prandtl (or Schmidt) number $Pr = 700$. We select four locations on the linear stability boundary: three qualitatively distinct Holmboe cases (having widely different Reynolds numbers Re, Richardson numbers J, steamwise wavenumbers k, and phase speeds), and one Kelvin-Helmholtz case to serve as a comparison. We produce supercritical bifurcation diagrams for each case, both in Re and J, and we find great differences in the scaling and magnitude of stable equilibrium branches, be it between Holmboe cases, between the Holmboe and Kelvin-Helmholtz cases, and between bifurcations in supercritical Re or J. We also study phase portraits to delve into the transient dynamics of the two counter-propagating Holmboe modes, and we find a special case in which specific initial conditions can lead to the non-monotonic growth or decay of individual modes. Next, we deconstruct the perturbation expansions to investigate in detail the spatial structures of all the component modes (linear and nonlinear), and highlight the underlying saturation mechanisms. We again find differences between Holmboe cases, and Re or J (such as the dominance of order 2 *vs* order 3 terms, and of various wavenumber harmonics $0, k, 2k, 3k$). Finally, we discuss the potential relevance of our analysis to recent experimental measurements of supercritical Holmboe waves, and its possible extension to asymmetric Holmboe waves to tackle the question of mode selection. We believe these results provide a basis for a future fully-nonlinear analysis of the Holmboe dynamical system.

I. INTRODUCTION

Stratified shear flows – Due to their physico-chemical heterogeneity, most environmental flows are stratified in density. The atmosphere and oceans are mostly *stably* stratified, *i.e.* their density tends to decrease with height (gravitational potential). Moreover, flows driven by buoyancy forces often have vertical shear, *i.e.* fluid layers at different densities tend to flow at different velocities. The complicated hydrodynamic stability properties of such stably-stratified shear flows control the presence and amplitude of waves, which in turn control the mixing and transport of heat, salt and other tracers between atmospheric and oceanic layers.

Nonlinear Holmboe waves – Focusing our attention on parallel shear flows with a single stable density interface, two distinct and contrasting types of linear instabilities stand out as particularly important. In the Kelvin-Helmholtz instability, a single mode of instability grows with zero phase speed (relative to the mean base flow). Its characteristic billows tend to grow to large enough amplitudes to overturn and trigger turbulence

---

* Corresponding author: lefauve@damtp.cam.ac.uk

and mixing, such that the instability is typically short-lived for a wide range of relevant parameters. By contrast, in the Holmboe instability, two modes of instability grow and travel with non-zero, opposite phase speeds. Its characteristic cusped waves tend to grow to moderate amplitudes and to actively preserve the sharp density interface on which they rely, such that the instability is typically long-lived [1]. In this paper, we seek to understand the nonlinear growth and saturation of the Holmboe instability, which controls its asymptotic finite-amplitude properties and therefore its long-lived geophysical properties.

Context – Over the last decades, Holmboe waves (defined here as being the long-lived, finite-amplitude waves originating from the linear Holmboe instability) have been the focus of numerous numerical and experimental studies. Direct numerical simulations (DNSs) in two and three dimensions have shed light on some aspects of their rich nonlinear behaviors, such as interaction between the two traveling waves, mixing of the density interface [1–7]. Laboratory experiments in salt-stratified exchange flows have also observed, measured, and attempted to explain and classify Holmboe waves [6, 8–10]. More recently, novel three-dimensional, volumetric measurements of the velocity and density fields have allowed to accurately measure the amplitude of these waves and to compare their spatial structure to linear stability predictions with excellent agreement [11, § 3.2], [12]. However, to the authors' knowledge, there exists no systematic investigation of the nonlinear saturation and observed amplitude of these waves, and in particular no nonlinear stability theory to compare numerical or experimental results against.

Motivation – This paper proposes to build the basis for such a theory by performing a weakly-nonlinear analysis of Holmboe waves, as suggested in [13]. Contrary to 'fully nonlinear' DNSs or experiments, our analysis is only 'weakly-nonlinear' in the sense that it considers only the 'weakest' nonlinearities necessary for a linear instability (of initially infinitesimal amplitude) to reach a stable, asymptotic finite amplitude (a process that we call 'nonlinear saturation'). Such a weakly-nonlinear analysis has a number of advantages, which make it well suited for an exploratory investigation of nonlinear stability. First, it elucidates, through its methodical and elegant construction, the specific nonlinear contributions responsible for nonlinear saturation. Second, although it is in principle valid only in a narrow region of parameter space (near the onset of linear instability, where nonlinearities are 'weak'), its low computational cost allows its practical implementation over its full range of validity (in contrast to fully nonlinear DNSs or experiments, which are 'valid everywhere', but whose cost prohibits their practical implementation over a wide range of parameters).

Supercritical vs *subcritical* – The field of nonlinear stability makes an important distinction between supercritical and subcritical bifurcations, depending on whether the finite-amplitude equilibrium branch of interest exists under supercritical conditions, *i.e.* for parameters where the base flow (zero-amplitude solution) is linearly unstable, or under subcritical conditions, *i.e.* for parameters where the base flow is linearly stable. In a *subcritical* pitchfork bifurcation, the finite-amplitude solution branch is unstable, and is therefore not expected to be observed either numerically or experimentally (at least close to the critical point, in the absence of a subcritical saddle-node bifurcation creating a further stable branch). Such a branch however reveals a (nonlinear) instability to finite-amplitude perturbations, which has a particular interest in explaining turbulent transitions in flows that are always linearly stable (*e.g.* Hagen-Poiseuille and plane Couette flows). By contrast, in a *supercritical* bifurcation, the finite-amplitude branch is stable, and is therefore expected to be observed numerically or experimentally, at least for parameters near the critical point. In this paper, we focus exclusively on supercritical bifurcations, as we seek to gain insight into the long-lived, finite-amplitude Holmboe waves found under linearly unstable conditions relevant to laboratory and geophysical applications. This focus has the additional advantage of ruling out the existence of complicated subcritical resonances (as we will explain later).

Previous weakly-nonlinear work – Weakly-nonlinear stability theory, even when restricted to the narrow class of parallel shear flows, is a rich area of research, dating back at least to the early ideas of Stuart [14], and formalized by the twin studies of Stuart [15] and Watson [16]. It has been applied to a variety of flows, notably to the unbounded free shear layer [17, 18], and to three bounded shear flows: plane Poiseuille flow ([15], etc), plane Couette flow ([16], etc), and Hagen-Poiseuille (pipe) flows ([19, 20], etc). Unbounded stratified shear layers have also received some attention, most notably in [21] and [22], who primarily studied the influence of stratification on the Kelvin-Helmholtz instability (their choice of base flows and parameter values did not support the Holmboe instability). Moreover, we note that most studies to date focused on subcritical bifurcations. We therefore propose to add to the current state of knowledge by carrying out the first weakly-nonlinear analysis of supercritical Holmboe waves.

Moreover, past weakly-nonlinear analyses had highly disparate formulations, making it exceedingly difficult to

obtain a unified picture of their results, which were besides rarely framed with applications to 'real' flows in mind. The choice of asymptotically small parameter varied between studies, which has non-trivial implications; some did not include, for simplicity, all nonlinear terms required at a particular order of the expansion; and some used other types of arcane simplifying assumptions and specific scaling laws causing a hazy loss of generality and applicability (see *e.g.* [23] and [24] for a comparison of different formulations). Recently Pham & Suslov [25] proposed an clear, elegant, and rigorous formulation which solves the above limitations, and Dey & Suslov [26] extended it to a pair of unstable modes, which is required in the Holmboe instability. We will therefore apply their formulation to our problem, in order to strive towards results that are more generally applicable and straightforward to interpret.

Objectives and outline – In § II we introduce our setup (equations, base flows, parameters). The next three sections §§ III-V address the three key objectives of this paper. In § III we develop a weakly-nonlinear formulation for Holmboe waves. In order to do so, we will first introduce a single-mode analysis (suited to Kelvin-Helmholtz), before building on it and introducing a double-mode analysis (suited to Holmboe). We will limit the scope of this paper to (i) the case of symmetric Holmboe waves, in which the mid-point of the velocity and density base flows are coincident; (ii) the inclusion of third-order nonlinearities necessary to obtain nonlinear saturation and supercritical pitchforks. However our formulation will be clear, robust and versatile enough to be readily generalizable to asymmetric Holmboe waves, and higher-order nonlinearities. In § IV we produce amplitude bifurcation diagrams in Reynolds and Richardson numbers for the supercritical Holmboe bifurcations in three distinctly different regions of parameter space. We also compare these Holmboe bifurcations to Kelvin-Helmholtz bifurcations. In § V we investigate the spatial structure of all terms in the nonlinear expansion to highlight the mechanisms responsible for nonlinear saturation. In § VI we conclude and suggest future directions.

II. SETUP

A. Governing equations

The fully nonlinear Navier-Stokes-Boussinesq equations are given non-dimensionally as:

$$\boldsymbol{\nabla} \cdot \boldsymbol{u} \; = \; 0, \tag{1a}$$

$$\partial_t \boldsymbol{u} + \boldsymbol{u} \cdot \boldsymbol{\nabla} \boldsymbol{u} \; = \; -\boldsymbol{\nabla} p + J \rho \, \hat{\boldsymbol{d}} \; + \frac{1}{Re} \, \boldsymbol{\nabla}^2 \boldsymbol{u}, \tag{1b}$$

$$\partial_t \rho + \boldsymbol{u} \cdot \boldsymbol{\nabla} \rho \; = \; \frac{1}{Re\,Pr} \, \boldsymbol{\nabla}^2 \rho. \tag{1c}$$

In the above, $\boldsymbol{u}(\boldsymbol{x},t) \equiv [u,w]^T$ is the two-dimensional velocity along $\boldsymbol{x} = [x,z]^T$, $\rho(\boldsymbol{x},t)$ is the density field, understood as a perturbation around the neutral density $\rho = 0$ (the buoyancy field $b \equiv -\rho$ is often used instead in the literature). We allow for the possibility of gravity to be inclined at an angle θ from the vertical of our coordinate system, resulting in $\hat{\boldsymbol{d}} = [\sin\theta, -\cos\theta]^T$. This is motivated by applications in which the flow is obtained by exchange through a channel inclined at an angle $\theta \geq 0$ from the horizontal (see [12] figure 1 and equation 5.1). The non-dimensional parameters Re, J, θ, Pr are discussed in § II D.

B. Base flow

The one-dimensional base flow around which we will investigate perturbations throughout this paper is:

$$\boldsymbol{u}_{00}(z) \equiv \begin{bmatrix} u_{00}(z) \\ w_{00}(z) \end{bmatrix} \equiv \begin{bmatrix} -\tanh z \\ 0 \end{bmatrix} \qquad \rho_{00}(z) \equiv -\tanh Rz, \tag{2}$$

where $\equiv$ denotes a definition. The corresponding square buoyancy frequency is $N_{00}^2 \equiv -J\partial_z \rho_{00} = JR \operatorname{sech}^2 Rz$ and the gradient Richardson number is $Ri_{g,00}(z) \equiv JR \operatorname{sech}^2 Rz / \operatorname{sech}^4 z$. Our choice of superscript $_{00}$ notation highlights the fact that the base flow is a contribution 'at order 0' (in powers of amplitude) and 'wavenumber 0' (streamwise invariant), as will be systematized in the next section. The minus sign in u_{00} is arbitrary and unimportant; it is retained purely for consistency with prior notation in [12].

We selected this smooth, hyperbolic tangent base flow (2) because it has been extensively used in the literature as a convenient and canonical mathematical model of stratified shear layers (*e.g.* [1, 27–29]). Requiring this base flow to be a steady-state solution of (1b)-(1c) will require additional forcing terms as we explain below.

C. Streamfunction and forcing

In the remainder of the paper, we adopt a streamfunction formulation. We define the usual scalar streamfunction $\psi(\boldsymbol{x}, t)$ as $\boldsymbol{u} \equiv [u, w]^T \equiv [\partial_z \psi, -\partial_x \psi]^T$, noting that the divergence-free condition (1a) is satisfied by construction.

Combining the x and z component of the momentum equation (1b), we obtain the evolution of the (negative) scalar vorticity $-\omega \equiv \partial_z u - \partial_x w = \boldsymbol{\nabla}^2 \psi$. Gathering linear terms on the left-hand side, and nonlinear terms on the right-hand side, we rewrite (1) as:

$$\partial_t(\boldsymbol{\nabla}^2 \psi) - J\,\hat{\boldsymbol{d}'} \cdot \boldsymbol{\nabla} \rho - \frac{1}{Re}\boldsymbol{\nabla}^4 \psi + \underbrace{J\sin\theta\,\partial_z \rho_{00} + \frac{1}{Re}\partial_{zzzz}\psi_{00}}_{\text{forcing}} = \underbrace{\partial_x \psi \partial_z(\boldsymbol{\nabla}^2 \psi) - \partial_z \psi \partial_x(\boldsymbol{\nabla}^2 \psi)}_{\text{convection (nonlinear)}} \quad (3a)$$

$$\partial_t \rho - \frac{1}{Re\,Pr}\boldsymbol{\nabla}^2 \rho + \underbrace{\frac{1}{Re\,Pr}\partial_{zz}\rho_{00}}_{\text{forcing}} = \underbrace{\partial_x \psi \partial_z \rho - \partial_z \psi \partial_x \rho}_{\text{advection (nonlinear)}} \quad (3b)$$

where $\hat{\boldsymbol{d}'} = [\cos\theta, \sin\theta]^T$. These two equations will form the basis of our theory in § III. The left-hand side 'forcing' terms are required by the implicit requirement that the base flow (2) satisfies the steady-state momentum and density equations (1b)-(1c) *i.e.* $\partial_t \psi = \partial_t \rho = 0$ when $\psi = \psi_{00} = \ln(\cosh z), \rho = \rho_{00} = -\tanh Rz$. These terms counteract diffusion of u_{00}, ρ_{00}, and acceleration of u_{00} when $\theta > 0$. Although necessary, these forcing terms rarely need to be explicitly written in simple, linear stability analyses, as they (by construction) vanish when solving for the evolution of perturbations. We write them here explicitly for completeness and greater transparency in the development of our weakly-nonlinear analyses in § III. Note that this forcing was used in the recent fully-nonlinear DNSs of [30] (see their 'Class S steady shear layer').

D. Parameters

The above model (2)-(3) has five non-dimensional parameters:

1. the Reynolds number Re measuring the inverse ratio of inertial over viscous time scales;

2. the bulk Richardson number J (also called Ri or Ri_b in the literature) measuring the inverse square ratio of buoyancy over shear time scales;

3. the title angle θ, set in this paper at $\theta = 0$ (for simplicity, noting that the role of θ on stability properties is poorly understood);

4. the Prandtl number Pr measuring the ratio of momentum to scalar diffusion, set in this paper at $Pr = 700$ (representing salt stratification, noting that the role of Pr on stability properties is poorly understood);

5. the ratio of velocity to density interface thickness R, set in this paper at $R = 5$ (representative of the salt-stratified experiments in which Holmboe waves are observed, *e.g.* in [12]).

To find out more about the link between the dynamical non-dimensional parameters Re, J and the dimensional experimental parameters (scales of velocity, length and density), the reader is referred to [12] (equations 3.4, 3.5, 5.1).

In the remainder of this paper, we gather these five parameters in a single parameter vector $\mathbf{Q}$:

$$\mathbf{Q} \equiv \begin{bmatrix} Re, J, \theta, Pr, R \end{bmatrix}^T \equiv \begin{bmatrix} Re, J, 0, 700, 5 \end{bmatrix}^T, \quad (4)$$

which we will only vary in the two dimensions of Re and J. These two parameters are well-known to be the two key parameters influencing the Kelvin-Helmholtz and Holmboe instabilities, and therefore constitute natural starting points to explore their nonlinear behaviors.

III. THEORY: WEAKLY-NONLINEAR ANALYSES

A. Method

Since the 1960s, a large number of (often subtly) different weakly-nonlinear methods have been employed. All methods ultimately rely on the choice of a small parameter used to construct an asymptotic series approximating the fully nonlinear solution (the Stuart-Landau series for the perturbation amplitude A introduced further down in (15)). The two most popular families of methods are (for a review, see [23], [25] § 1 and references therein):

1. *Multiscale expansions*, in which the expansion parameter is $||\mathbf{Q} - \mathbf{Q}_c||/||\mathbf{Q}_c||$, the relative parametric distance away from the critical point $\mathbf{Q}_c$ at which linear instability first appears (method first introduced by [15]). The resulting multiple timescale expansion enforces a specific, rigid scaling of the solution near $||\mathbf{Q}_c||$ (in particular a linear growth rate) which is only expected to hold very near $||\mathbf{Q}_c||$. The validity of this method is therefore not guaranteed away from the critical point, which is primarily why we did not employ it.

2. *Amplitude expansions*, in which the expansion parameter is the magnitude of the perturbation amplitude $|A|$ itself (method first introduced by Watson [16]). This parameter does not enforce any specific scaling on the solution and can be applied near and away from $||\mathbf{Q}_c||$. The validity of this method is guaranteed *a posteriori* as long as $|A|$ remains small enough. Near $\mathbf{Q}_c$, the multiscale and amplitude expansions method are formally equivalent. Away from $\mathbf{Q}_c$, the amplitude expansion method is ambiguous and requires an additional constraint to guarantee a unique solution $|A|$, whose application and interpretation have been recently made straightforward [25]. It is essentially this method that we employ in this paper.

Our amplitude expansion takes fundamentally different forms depending on whether the linearized equations admit a single unstable mode (Kelvin-Helmholtz instability), or a couple of complex conjugate modes (Holmboe instability), which are the first-order perturbations in our expansion. We therefore need to treat each case separately, and start with the simpler single-mode analysis in § III B, before building on it to develop the double-mode analysis in § III C. For succinct summaries and schematics of the solution algorithm, we refer the impatient reader directly to § III B 6, figure 1 (single mode), and § III C 6, figure 2 (double mode).

B. Single-mode analysis (Kelvin-Helmholtz instability)

1. Order 1 perturbation

Expansion – We start with a first order (hereafter 'order 1') perturbation in our amplitude expansion:

$$\psi(x, z, t) = \psi_{00}(z) + \left\{ A(t)\psi_{11}(z)E(x) + \text{c.c.} \right\}, \tag{5a}$$

$$\rho(x, z, t) = \rho_{00}(z) + \left\{ A(t)\rho_{11}(z)E(x) + \text{c.c.} \right\}, \tag{5b}$$

where the x-dependence is $E = e^{ikx}$, with $k \in \mathbb{R}_+^*$. Note that the total flow and the base flow are real ($\psi, \rho, \psi_{00}, \rho_{00} \in \mathbb{R}$), while the amplitudes and vertical structures are generally complex ($A, \psi_{mn}, \rho_{mn} \in \mathbb{C}$ for $n, m > 0$), which is why we always add the complex conjugate (c.c.) of any complex terms.

Throughout § III B, the subscripts $_{mn}$ denote a vertical mode factored by a temporal amplitude of order m, i.e. $A^m(t)$, and streamwise wavenumber nk, i.e. $E^n = e^{inkx}$. In particular, this highlights the interpretation of our base flow $[\psi_{00}, \rho_{00}]$ as a mode with temporally steady amplitude $A^0(t) = 1$ and streamwise invariant structure $E^0(x) = 1$.

Defining our flow state vector as $\mathbf{w} = [\psi, \rho]^T$ (and similarly for all subscripts $_{mn}$) we rewrite (5) in shorthand as:

$$\mathbf{w}(x, z, t) = \mathbf{w}_{00}(z) + \left\{ A(t)\mathbf{w}_{11}(z)E(x) + \text{c.c.} \right\}. \tag{6}$$

Evolution – Substituting (5) into our nonlinear equations (3) and neglecting any terms of order $m > 1$, we

obtain the order 1 (linear) evolution:

$$\frac{dA}{dt}(\psi_{11}'' - k^2\psi_{11})E = A\Big\{ J\sin\theta\rho_{11}' + ikJ\cos\theta\rho_{11} \tag{7a}$$

$$+ \frac{1}{Re}(\psi_{11}^{(4)} - 2k^2\psi_{11}'' + k^4\psi_{11}) - ik\psi_{00}'(\psi_{11}'' - k^2\psi_{11}) + ik\psi_{00}'''\psi_{11}\Big\}E$$

$$\frac{dA}{dt}\rho_{11}E = A\frac{1}{RePr}\Big\{(\rho_{11}'' - k^2\rho_{11}) + ik\rho_{00}'\psi_{11} - ik\psi_{00}'\rho_{11}\Big\}E, \tag{7b}$$

where $'$ denotes differentiation with respect to the only variable z. In matrix notation, this reduces to:

$$\frac{dA}{dt}\mathscr{A}_k\mathbf{w}_{11} = A\,\mathscr{B}_{k,\mathbf{Q}}\mathbf{w}_{11}, \tag{8}$$

where the left-hand side and right-hand side linear differential operators $\mathscr{A}_k, \mathscr{B}_{k,\mathbf{Q}} \in \mathbb{C}$ are given in the Appendix B 1 (equation (B1)). They are indexed by k and $\mathbf{Q}$ to highlight their dependence on the wavenumber k and parameter vector $\mathbf{Q}$ (defined earlier in (4)).

Eigenvalue problem – This differential system is soluble only if $d_t A = \sigma A$ such that:

$$\boxed{\mathscr{L}_{k,\sigma,\mathbf{Q}}\mathbf{w}_{11} = (\mathscr{B}_{k,\mathbf{Q}} - \sigma\mathscr{A}_k)\mathbf{w}_{11} = 0}, \tag{9}$$

where we defined the linear operator $\mathscr{L}_{k,\sigma,\mathbf{Q}} \equiv \mathscr{B}_{(k,\mathbf{Q})} - \sigma\mathscr{A}_k$ (see (B2)-(B3) for the full expression). Therefore $\sigma \in \mathbb{C}$ and $\mathbf{w}_{11} \in \mathbb{C}$ are eigenvalues and eigenvectors of the generalised eigenvalue problem for $\mathscr{A}_k, \mathscr{B}_{k,\mathbf{Q}}$, describing the temporal stability of the perturbation.

Mode symmetries – We note that there is an important symmetry to these equations: if $\psi(z), \rho(z)$ are solutions with eigenvalue σ, then $\psi^*(-z), -\rho^*(-z)$ are solutions with eigenvalue σ^*, which we summarize by the expression

$$\{\psi(z), \rho(z), \sigma\} \to \{\psi^*(-z), -\rho^*(-z), \sigma^*\}. \tag{10}$$

In the single-mode analysis of this section, we consider the case of a single real eigenvalue $\sigma = \sigma_r \in \mathbb{R}$ and single eigenmode $\mathbf{w}_{11}$. In the double-mode analysis of the next section § III C, we will consider a pair of complex conjugate eigenvalues and eigenmodes, and will impose this complex conjugate symmetry condition exactly in order to improve the accuracy of solutions.

2. Order 2 perturbation

Expansion – We extend the perturbation expansion (6) to order 2 in order to take into account the first nonlinear effects:

$$\mathbf{w}(x,z,t) = \mathbf{w}_{00}(z) + \underbrace{|A(t)|^2\mathbf{w}_{20}(z)}_{\text{new term}} + \Big\{ A(t)\mathbf{w}_{11}(z)E(x) + \underbrace{A^2(t)\mathbf{w}_{22}(z)E^2(x)}_{\text{new term}} + \text{c.c.}\Big\}. \tag{11}$$

The two new order 2 terms ($m = 2$) are: $\mathbf{w}_{20}$ corresponding to a distortion (or 'feedback') on the mean flow ($n = 0$), and $\mathbf{w}_{22}$ corresponding to the second harmonic ($n = 2$). Note the distinction between the original *base* flow $\mathbf{w}_{00}(z)$, and the resulting *mean* flow at order 2 $\mathbf{w}_{00}(z) + |A|^2\mathbf{w}_{20}(z)$.

For a summary of the terms $\mathbf{w}_{mn}$ required by the nonlinearity of the Navier-Stokes equations at successively higher orders $m = 2, 3, \dots$ see Appendix A 1 (table III).

Evolution – Substituting our expansion (11) into the nonlinear equation (3) and collecting like terms we get a system of equations which we again reduce to a matrix form, using the same operator $\mathscr{L}$ (defined in (9), (B2), (B3)) but with modified arguments since $d_t|A|^2 = 2\sigma_r$ and $d_t A^2 = 2\sigma$:

$$\boxed{\mathscr{L}_{0,2\sigma_r,\mathbf{Q}}\mathbf{w}_{20} = \mathbf{f}_{20}} \quad \text{and} \quad \boxed{\mathscr{L}_{2k,2\sigma,\mathbf{Q}}\mathbf{w}_{22} = \mathbf{f}_{22}}, \tag{12}$$

where the forcing terms $\mathbf{f}_{20}, \mathbf{f}_{22}$ are given in the Appendix B 1 (equation (B4)). The two linear operators in (12) are non-singular, and therefore invertible, even in the limit $\mathbf{Q} \to \mathbf{Q}_c, \sigma_r \to 0^+$, so these equations always have unique solutions $\mathbf{w}_{20}, \mathbf{w}_{22}$ [25]. All equations that are boxed are key in the solution algorithm.

3. Order 3 perturbation

Extending the perturbation to order 3, we have (see Appendix A 1, table III):

$$\mathbf{w} = \mathbf{w}_{00} + |A|^2\mathbf{w}_{20} + (A\mathbf{w}_{11}E + A^2\mathbf{w}_{22}E^2 + \underbrace{A|A|^2\mathbf{w}_{31}E + A^3\mathbf{w}_{33}E^3}_{\text{new terms}} + \text{c.c.}). \tag{13}$$

Substituting into (3) and collecting like terms, we get:

$$\boxed{\mathscr{L}_{k,\sigma+2\sigma_r,\mathbf{Q}}\mathbf{w}_{31} = \mathbf{f}_{31}} \quad \text{and} \quad \boxed{\mathscr{L}_{3k,3\sigma,\mathbf{Q}}\mathbf{w}_{33} = \mathbf{f}_{33}}. \tag{14}$$

In the subcritical bifurcations (not treated in this paper), [25] noted that when $\sigma_r < 0$, the operator $\mathscr{L}_{k,\sigma+2\sigma_r,\mathbf{Q}}$ can in principle be singular, which would signal the existence of resonances beween decaying instability modes that need to be solved separately [19, 31], adding complexity to the solution and its interpretation.

In the supercritical bifurcations (treated in this paper) subcritical resonances are fortunately always ruled out. Instead, care needs to be exercised only in the limit $\mathbf{Q} \to \mathbf{Q}_C, \sigma_r \to 0$, since $\mathscr{L}_{k,\sigma+2\sigma_r,\mathbf{Q}} \to \mathscr{L}_{k,\sigma,\mathbf{Q}_C}$, which by construction is singular (see (9)) and does not admit a solution $\mathbf{w}_{31}$. This singularity is treated next.

4. Landau coefficient

Stuart-Landau equation – To resolve the singularity in (14) (for $\mathbf{w}_{31}$), we assume (without *a priori* justification) that we can write the following Stuart-Landau evolution equation:

$$\frac{dA}{dt} = \sigma A + KA|A|^2 + \dots, \tag{15}$$

i.e. an asymptotic series that can be truncated after some finite number of terms, here after the first Landau coefficient K. This does not affect the problem in (9) (for $\mathbf{w}_{11}$) or in (12) (for $\mathbf{w}_{20}, \mathbf{w}_{22}$), nor indeed to the second problem in (14) (for $\mathbf{w}_{33}$). However, the problem in (14) (for $\mathbf{w}_{31}$) now reads:

$$\mathscr{L}_{k,\sigma+2\sigma_r,\mathbf{Q}}\mathbf{w}_{31} = -K\mathscr{A}_k\mathbf{w}_{11} + \mathbf{f}_{31}, \tag{16}$$

due to an additional term that had been neglected in (9).

Solution method – Near the critical point (in the limit $\mathbf{Q} \to \mathbf{Q}_C, \sigma_r \to 0$) $\mathscr{L}_{k,\sigma+2\sigma_r,\mathbf{Q}}$ is singular and a unique solution $\boldsymbol{w}_{31}$ exists only for a specific K, classically obtained by enforcing a solvability condition involving the adjoint problem of (9) as explained in Appendix D.

However, it was found in practice that, for the problems solved in this paper, the solvability condition could be replaced in favor of a more straightforward and efficient method described in Pham & Suslov [25] and summarized below.

Away from the critical point $\mathscr{L}_{k,\sigma+2\sigma_r,\mathbf{Q}}$ is non-singular and a unique solution $\mathbf{w}_{31}$ exists for any choice of K. This ambiguity in K is resolved by enforcing a (weighted) orthogonality condition between $\mathbf{w}_{11}$ and $\mathbf{w}_{31}$ (the order 1 and order 3 modes at the fundamental wavenumber k):

$$\langle \mathbf{w}_{11}, \mathbf{w}_{31} \rangle_{\mathscr{M}} \equiv \mathbf{w}_{11}^H \cdot \mathscr{M}\mathbf{w}_{31} = 0, \tag{17}$$

where ^{H} denotes the Hermitian (or conjugate) transpose. The matrix $\mathscr{M}$ is a positive-definite Hermitian matrix which essentially selects a low-dimensional projection of the solution. In this work, we chose $\mathscr{M}$ to represent the total (kinetic + scalar) energy norm, as explained in Appendix C. This integral measure has the advantage of using all components of $\mathbf{w}$, and making our results readily comparable with DNSs or recent experimental measurements (such as those of [32]). As explained in [25] § 4, a different choice of $\mathscr{M}$ would yield results viewed under a different – but equally valid – angle (such an analysis is beyond the scope of this paper).

The extended system (16)-(17) for $\mathbf{w}_{31}$ is then given by:

$$\boxed{\hat{\mathscr{L}}_{31}\,\hat{\mathbf{w}}_{31} = \hat{\mathbf{f}}_{31}}, \tag{18}$$

where the hat variables have an additional row:

$$\hat{\mathscr{L}}_{31} = \begin{bmatrix} \mathscr{L}_{k,\sigma,\mathbf{Q}} - 2\sigma_r \mathscr{A}_k & \mathscr{A}_k \mathbf{w}_{11} \\ \mathbf{w}_{11}^H \mathscr{M} & 0 \end{bmatrix}, \quad \hat{\mathbf{w}}_{31} = \begin{bmatrix} \mathbf{w}_{31} \\ K \end{bmatrix}, \quad \hat{\mathbf{f}}_{31} = \begin{bmatrix} \mathbf{f}_{31} \\ 0 \end{bmatrix}. \tag{19}$$

The operator $\hat{\mathscr{L}}_{31}$ is always non-singular, but may be poorly conditioned near the critical point, in which case the solvability condition in Appendix D should be used. However, in our work, it was found to remain sufficiently well-conditioned to be inverted reliably and give $\mathbf{w}_{31}$ and K.

5. Equilibrium amplitude

The equilibrium amplitude (implicitly taken as its modulus $|A_e| > 0$) is found when the truncated Stuart-Landau series (15) reaches steady-state, or:

$$\left(\frac{1}{|A|^2} \frac{d|A|^2}{dt} \right)_e = 2\sigma_r + 2K|A_e|^2 = 0 \quad \Longrightarrow \quad \boxed{|A_e| = \sqrt{-\frac{\sigma_r}{K}}}. \tag{20}$$

One of the main results of the above analysis is a bifurcation diagram: the variation of $|A_e|$ as the bifurcation parameter $\mathbf{Q}$ is varied away from the critical point $\mathbf{Q}_c$, and the $|A_e| = 0$ solution becomes unstable.

In this paper we only consider supercritical bifurcations, in which $\sigma_r > 0, K < 0$ and therefore $d_t|A|^2 \gtrless 0$ for $|A| \lessgtr |A_e|$ making it a stable, or attracting, solution. In other words, the weak nonlinearities embedded in the Landau coefficient saturate the linear instability by negative feedback.

The validity of our amplitude expansion must be assessed *a posteriori*. The solution is valid only if $|A_e|$ remains sufficiently small so that its successive powers decay fast enough ($|A_e|^{2m+2} \ll |A_e|^{2m}$, $m = 0, 1, \ldots$) for the Stuart-Landau series to be meaningfully truncated (subject to the hope that the next Landau coefficient is not exceedingly large). In our numerical computations, we imposed an additional criterion for the validity of the procedure, that the total energy of the perturbation (given by A_e but also all $\mathbf{w}_{mn}$) remains small compared to that of the base flow $\mathbf{w}_{00}$ (more details in our results section § IV).

6. Algorithm

Figure 1 summarizes the above single-mode algorithm used in the numerical solution of the problem. The key equations to solve are boxed in the above section and in the figure: (9) (eigenvalue problem), (12), (14), (18) (matrix inversions), and (20). One feature that is worth emphasizing here is that, for each successive value of the parameter $\mathbf{Q}$, the eigenvalue problem (9) ('Order 1' top box in figure 1) is solved over a range of wavenumbers k in order to find the maximum σ_r (which requires high resolution in k near $\mathbf{Q}_c$, where $\sigma_r \gtrsim 0$).

The numerical implementation, including the discretization of the problem and the boundary conditions are discussed in § III D. The results of this analysis applied to Kelvin-Helmholtz supercritical bifurcations are discussed in §§ IV-V.

C. Double-mode analysis (Holmboe instability)

1. Expansion and Stuart-Landau equations

We now extend the above single-mode analysis to the case of two complex conjugate dominant modes, adapted to the symmetric Holmboe instability. Instead of deriving the expansion step by step as in the single-mode
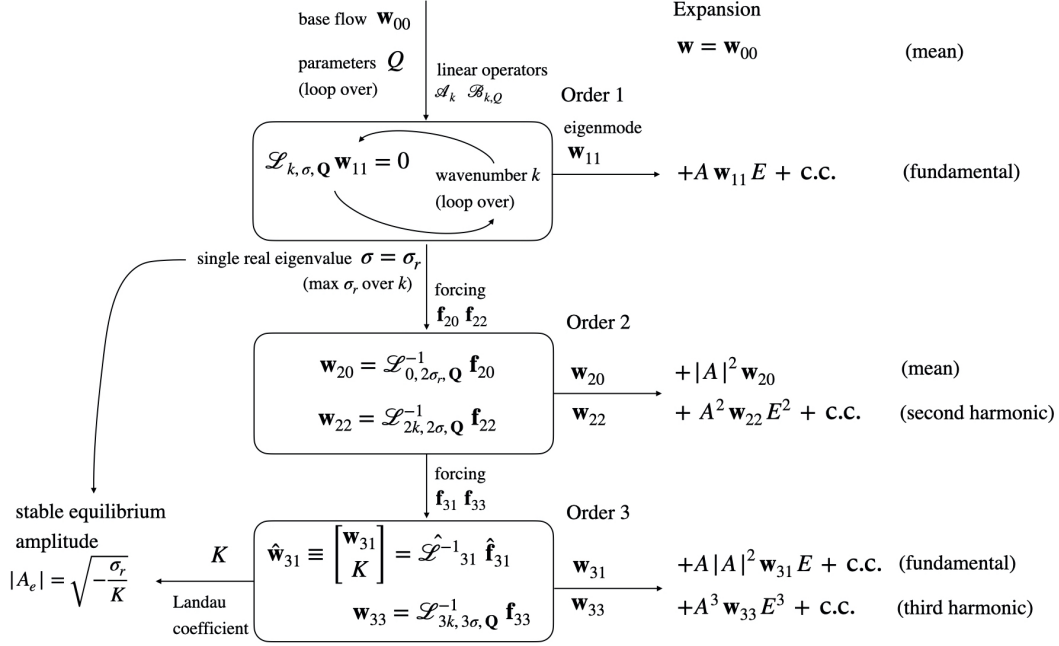
FIG. 1: Algorithm to obtain the single-mode (Kelvin-Helmholtz) expansion and equilibrium amplitude (summarizing § III B).

analysis, we follow [26] and seek a solution of the form:

$$
\mathbf{w}(x, z, t) = \mathbf{w}_{000} + \left\{ A_{200}^{(1)} \mathbf{w}_{200}^{(1)} + A_{200}^{(2)} \mathbf{w}_{200}^{(2)} \right\}
$$

$$
+ \left\{ (A_{110} \mathbf{w}_{110} E_1 + A_{101} \mathbf{w}_{101} E_2) + \right.
$$

$$
(A_{21-1} \mathbf{w}_{21-1} E_1 E_2^* + A_{220} \mathbf{w}_{220} E_1^2 + A_{202} \mathbf{w}_{202} E_2^2 + A_{211} \mathbf{w}_{211} E_1 E_2) +
$$

$$
\left. (A_{310}^{(1)} \mathbf{w}_{310}^{(1)} E_1 + A_{310}^{(2)} \mathbf{w}_{310}^{(2)} E_1 + A_{301}^{(1)} \mathbf{w}_{301}^{(1)} E_2 + A_{301}^{(2)} \mathbf{w}_{301}^{(2)} E_2) + \text{c.c.} \right\}, \tag{21}
$$

where the subscripts $_{mno}$ allow for an explicit interpretation of each term as being of order m in amplitude and with powers n and o of Fourier components $E_1^n = e^{ink_1 x}$ and $E_2^o = e^{iok_2 x}$. Note that although $E_1 = E_2 = e^{ikx}$ in our case, since symmetric Holmboe modes have identical wavenumber $k = k_1 = k_2$, we track $E_{1,2}$ separately for clarity of interpretation and in order to allow for a potential future extension to the asymmetric Holmboe instability having different wavenumbers $k_1 \neq k_2$ (maximizing σ_{r1}, σ_{r2}). We also note that the base flow remains identical: $\mathbf{w}_{000} = \mathbf{w}_{00}$.

Importantly, (21) contains all necessary order 2 terms, but has been conveniently truncated at order 3. In the single-mode analysis, we indeed saw that the order 3 fundamental contribution $\mathbf{w}_{31}$ was sufficient to obtain the Landau coefficient K and equilibrium amplitude $|A_e|$, which are our main focus (the third harmonic $\mathbf{w}_{33}$ was not necessary). Similarly, in the double-mode analysis, the order 3 fundamental contributions $\mathbf{w}_{310}^{(j)}, \mathbf{w}_{301}^{(j)}$ included in (21) are sufficient to obtain the Landau coefficients (the numerous remaining order 3 contributions are ignored here for simplicity). For more details on how the hierarchy of order 2 and order 3 terms are generated by nonlinearities, see Appendix A 2, tables IV-V, and the graph in figure 10.

We identify the amplitude of mode 1 and 2 respectively as $A_{1,2} \equiv A_{110,101}$ (shorthand notation) and we seek truncated Stuart-Landau evolution equations of the form:

$$
\frac{dA_1}{dt} = \sigma_1 A_1 + K_{11} A_1 |A_1|^2 + K_{12} A_1 |A_2|^2, \tag{22a}
$$

$$
\frac{dA_2}{dt} = \sigma_2 A_2 + K_{21} A_2 |A_1|^2 + K_{22} A_2 |A_2|^2, \tag{22b}
$$

where $\sigma_{1,2} = \sigma_r \pm \sigma_i$ are the two complex conjugate eigenvalues, and $K_{11}, K_{12}, K_{21}, K_{22}$ are the four Landau coefficients (K_{11}, K_{22} describe mode self-interactions, whereas K_{12}, K_{22} describe mode coupling).

In the following, we proceed by solving at each order of amplitude $m = 1, 2, 3$, collecting terms with the same Fourier components n, o at each stage. Much of the work in deriving the relevant operators was done in the single-mode analysis. Throughout this section, $\mathscr{A}_k$ and $\mathscr{B}_k, \mathscr{L}_{k,\sigma}$ are defined identically (see (B1)-(B3)), with the dependence of $\mathscr{B}$ and $\mathscr{L}$ on $\mathbf{Q}$ implicit to simplify the notation.

2. Order 1 perturbation

At first order, there is no mode interaction and so we recover two independent copies of the single-mode linear equation (9):

$$(A_{110}\mathscr{B}_k - \frac{dA_{110}}{dt}\mathscr{A}_k)\mathbf{w}_{110} = 0, \tag{23}$$

$$(A_{101}\mathscr{B}_k - \frac{dA_{101}}{dt}\mathscr{A}_k)\mathbf{w}_{101} = 0. \tag{24}$$

For these equations to be consistent, we must have

$$\frac{dA_{1,2}}{dt} = \sigma_{1,2}A_{1,2}, \tag{25}$$

where $\sigma_{1,2}$ are the complex conjugate eigenvalues of $\mathscr{L}_{k,\sigma} \equiv \mathscr{B}_k - \sigma\mathscr{A}_k = 0$, as shown in the single-mode analysis (9).

3. Order 2 perturbation

At second order, we recover mean flow and second harmonic contributions (two each, as opposed to one in the single-mode analysis), as well as new interaction terms (breather and mixed modes).

Mean flow E_j^0 – We have two contributions:

$$(A_{200}^{(j)}\mathscr{B}_0 - \frac{dA_{200}^{(j)}}{dt}\mathscr{A}_0)\mathbf{w}_{200}^{(j)} = |A_j|^2\mathbf{f}_{200}^{(j)} \quad \text{for } j = 1, 2, \tag{26}$$

where the index (j) refers to contribution of mode j to a term in $mno = 200$ (we recall our shorthand notation that mode 1 is '110' and mode 2 is '101'). The full expressions for the forcing terms $\mathbf{f}_{200}^{(j)}$ are given in Appendix B 2, equation (B6). The form of (26) along with (25) leads to:

$$A_{200}^{(j)} = |A_j|^2 \implies \frac{dA_{200}^{(j)}}{dt} = 2\sigma_r|A_j|^2 \implies \boxed{\mathscr{L}_{0,2\sigma_r}\mathbf{w}_{200}^{(j)} = \mathbf{f}_{200}^{(j)} \text{ for } j = 1, 2}. \tag{27}$$

Second harmonics E_j^2 – By the independent self-interaction of each mode, we have:

$$(A_{220}\mathscr{B}_{2k} - \frac{dA_{220}}{dt}\mathscr{A}_{2k})\mathbf{w}_{220} = A_1^2\mathbf{f}_{220} \tag{28a}$$

$$(A_{202}\mathscr{B}_{2k} - \frac{dA_{202}}{dt}\mathscr{A}_{2k})\mathbf{w}_{202} = A_2^2\mathbf{f}_{202}, \tag{28b}$$

where the forcing terms are given in (B7). The form of (28) gives

$$A_{220} = A_1^2 \implies \frac{dA_{220}}{dt} = 2\sigma_1 A_1^2 \implies \boxed{\mathscr{L}_{2k,2\sigma_1}\mathbf{w}_{220} = \mathbf{f}_{220}}, \tag{29a}$$

$$A_{202} = A_2^2 \implies \frac{dA_{202}}{dt} = 2\sigma_2 A_2^2 \implies \boxed{\mathscr{L}_{2k,2\sigma_2}\mathbf{w}_{202} = \mathbf{f}_{202}}. \tag{29b}$$

Breather mode $E_1 E_2^*$ – We have:

$$(A_{21-1}\mathscr{B}_0 - \frac{dA_{21-1}}{dt}\mathscr{A}_0)\mathbf{w}_{21-1} = A_1 A_2^* \mathbf{f}_{21-1}, \tag{30}$$

where the forcing term is given in (B8). The form of (30) gives:

$$A_{21-1} = A_1 A_2^* \implies \frac{dA_{21-1}}{dt} = (\sigma_1 + \sigma_2^*)A_1 A_2^* = 2\sigma_1 A_1 A_2^* \implies \boxed{\mathscr{L}_{0,2\sigma_1}\mathbf{w}_{21-1} = \mathbf{f}_{21-1}}. \tag{31}$$

Note that the conjugate mode $E_1^* E_2$ is implictly accounted for in the complex conjugate in (21). In the case of symmetric Holmboe modes $E_1 E_2^* = 1$; in other words this 'breather' mode (as it is called in the literature) is simply a mean flow contribution.

Mixed mode $E_1 E_2$ – We have:

$$(A_{211}\mathscr{B}_{2k} - \frac{dA_{211}}{dt}\mathscr{A}_{2k})\mathbf{w}_{211} = A_1 A_2 \mathbf{f}_{211}, \tag{32a}$$

where the forcing term is given in (B9). The form of (32a) gives:

$$A_{211} = A_1 A_2 \implies \frac{dA_{211}}{dt} = (\sigma_1 + \sigma_2)A_1 A_2 = 2\sigma_r A_1 A_2 \implies \boxed{\mathscr{L}_{2k,2\sigma_r}\mathbf{w}_{211} = \mathbf{f}_{211}}. \tag{33}$$

4. Order 3 perturbation

At order 3, we only focus on the fundamental contributions (in E_1 and in E_2) in order to obtain the Landau coefficients.

Fundamental E_1 – We have:

$$(A_{310}\mathscr{B}_k - \frac{dA_{310}}{dt}\mathscr{A}_k)\mathbf{w}_{310} = A_1|A_1|^2\mathbf{f}_{310}^{(1)} + A_1|A_2|^2\mathbf{f}_{310}^{(2)} - (K_{11}A_1|A_1|^2 + K_{12}A_1|A_2|^2)\mathscr{A}_k\mathbf{w}_{110}, \tag{34}$$

which we split into two equations which must both be satisfied:

$$(A_{310}^{(j)}\mathscr{B}_k - \frac{dA_{310}^{(j)}}{dt}\mathscr{A}_k)\mathbf{w}_{310}^{(j)} = A_1|A_j|^2(\mathbf{f}_{310}^{(j)} - K_{1j}\mathscr{A}_k\mathbf{w}_{110}) \quad \text{for } j = 1,2. \tag{35}$$

This form gives:

$$A_{310}^{(j)} = A_1|A_j|^2 \implies \frac{dA_{310}^{(j)}}{dt} = \sigma_j + 2\sigma_r \implies \mathscr{L}_{k,\sigma_1+2\sigma_r}\mathbf{w}_{310}^{(j)} = \mathbf{f}_{310}^{(j)} - K_{1j}\mathscr{A}_k\mathbf{w}_{110} \quad \text{for } j = 1,2. \tag{36}$$

The K_{1j} can be specified by imposing the orthogonality condition $\langle \mathbf{w}_{110}, \mathbf{w}_{310}^{(j)}\rangle_{\mathscr{M}} = 0$. As shown in the single-mode analysis (18), this is equivalent to solving the extended system

$$\boxed{\hat{\mathscr{L}}_{310}\hat{\mathbf{w}}_{310}^{(j)} = \hat{\mathbf{f}}_{310}^{(j)} \quad \text{for } j = 1,2}, \tag{37}$$

where

$$\hat{\mathscr{L}}_{310} = \begin{bmatrix} \mathscr{L}_{k,\sigma,\mathbf{Q}} - 2\sigma_r\mathscr{A}_k & \mathscr{A}_k\mathbf{w}_{110} \\ \mathbf{w}_{110}^H\mathscr{M} & 0 \end{bmatrix}, \quad \hat{\mathbf{w}}_{310}^{(j)} = \begin{bmatrix} \mathbf{w}_{310}^{(j)} \\ K_{1j} \end{bmatrix}, \quad \hat{\mathbf{f}}_{310}^{(j)} = \begin{bmatrix} \mathbf{f}_{310}^{(j)} \\ 0 \end{bmatrix}. \tag{38}$$

Fundamental E_2 – By analogy, we have:

$$\boxed{\hat{\mathscr{L}}_{301}\hat{\mathbf{w}}_{301}^{(j)} = \hat{\mathbf{f}}_{301}^{(j)} \quad \text{for } j = 1,2}, \tag{39}$$

where

$$\hat{\mathscr{L}}_{301} = \begin{bmatrix} \mathscr{L}_{k,\sigma,\mathbf{Q}} - 2\sigma_r\mathscr{A}_k & \mathscr{A}_k\mathbf{w}_{101} \\ \mathbf{w}_{101}^H\mathscr{M} & 0 \end{bmatrix}, \quad \hat{\mathbf{w}}_{301}^{(j)} = \begin{bmatrix} \mathbf{w}_{301}^{(j)} \\ K_{2j} \end{bmatrix}, \quad \hat{\mathbf{f}}_{301}^{(j)} = \begin{bmatrix} \mathbf{f}_{301}^{(j)} \\ 0 \end{bmatrix}. \tag{40}$$

The four Landau coefficients of (22) are obtained by solving (37), (39).

5. Equilibrium amplitudes

We return to the Stuart-Landau equations (22), which we recast in polar form by writing $A_j \equiv |A_j| e^{i\varphi_j}$. Upon cancelling the $e^{i\varphi_j}$ factors and taking real ($\Re$) and imaginary ($\Im$) parts, we obtain:

$$\frac{d|A_j|}{dt} = |A_j| \left\{ \sigma_r + \Re(K_{j1})|A_1|^2 + \Re(K_{j2})|A_2|^2 \right\} \qquad \text{for } j = 1, 2, \tag{41a}$$

$$\frac{d\varphi_j}{dt} = \sigma_i + \Im(K_{j1})|A_1|^2 + \Im(K_{j2})|A_2|^2 \qquad \text{for } j = 1, 2. \tag{41b}$$

We recall the Holmboe symmetry (10), which, when tracked through the whole series expansion, gives $K_{11} = K_{22}^*$ and $K_{12} = K_{21}^*$. Defining $\kappa_1 \equiv \Re(K_{11})$ and $\kappa_2 \equiv \Re(K_{12})$ (shorthand notation), (41a) becomes:

$$\frac{1}{|A_1|} \frac{d|A_1|}{dt} = \sigma_r + \kappa_1 |A_1|^2 + \kappa_2 |A_2|^2, \tag{42a}$$

$$\frac{1}{|A_2|} \frac{d|A_2|}{dt} = \sigma_r + \kappa_2 |A_1|^2 + \kappa_1 |A_2|^2. \tag{42b}$$

Note that (42) describes a two-dimensional dynamical system, where σ_r, κ_1 and κ_2 are complicated functions of the parameters $\mathbf{Q}$. We obtain a bifurcation diagram for $|A_1|, |A_2|$ by varying $\mathbf{Q}$ and assessing the stability of the four equilibrium solutions (fixed points), by inspecting the eigenvalues of the Jacobian of (42) in a supercritical scenario ($\sigma_r > 0$). The results are in table I and can be described as follows.

TABLE I: Equilibrium solutions and stability conditions for symmetric Holmboe modes.

Name	Mode 1 amplitude $|A_{1e}|$	Mode 2 amplitude $|A_{2e}|$	Stability conditions	Type for $\sigma_r > 0$
(i)	0	0	$\sigma_r < 0$	Unstable star
(ii)	0	$\sqrt{-\dfrac{\sigma_r}{\kappa_1}}$	$\sigma_r > 0, \ \kappa_2 < \kappa_1 < 0$	Saddle
(iii)	$\sqrt{-\dfrac{\sigma_r}{\kappa_1}}$	0	$\sigma_r > 0, \ \kappa_2 < \kappa_1 < 0$	Saddle
(iv)	$\sqrt{-\dfrac{\sigma_r}{\kappa_1 + \kappa_2}}$	$\sqrt{-\dfrac{\sigma_r}{\kappa_1 + \kappa_2}}$	$\sigma_r > 0, \ \kappa_1 < 0, \ |\kappa_2| < |\kappa_1|$	Stable node

Symmetric Holmboe waves – Symmetry requires that $\kappa_1 < 0$ and $|\kappa_2| < |\kappa_1|$ because (ii)-(iii) must be saddles, while solution (iv) must be stable. In other words, although different initial conditions $|A_1(0)| \neq |A_2(0)| \neq 0$ will lead to generally different finite-time amplitudes $|A_1| \neq |A_2|$, asymptotically the only stable (relevant) equilibrium (iv) has equal amplitudes $|A_{1e}| = |A_{2e}| = |A_e| = \sqrt{-\sigma_r/(\kappa_1 + \kappa_2)}$, while equilibria (ii) and (iii) can only be approached if $|A_1(0)| = 0$ or $|A_2(0)| = 0$ respectively. Futhermore, the reflectional symmetry of the vector field in the $(|A_1|, |A_2|)$ phase space on either side of the $|A_1| = |A_2|$ line requires that (iv) is a stable node (rather than a focus/spiral), as summarized in table I.

Asymmetric Holmboe waves – The linear operators $\mathscr{L}$ and forcing terms $\mathbf{f}$ would need to be changed throughout §§ III C 2-III C 4 to reflect the fact that $k_1 \neq k_2$, $\sigma_{1r} \neq \sigma_{2r}$, $\sigma_{1i} \neq -\sigma_{2i}$. However, we expect the dynamical system for $|A_1|, |A_2|$ to be of the same form as (41a) (replacing σ_r by σ_{1r}, σ_{2r} and retaining all four K_{ij} instead of the two $\kappa_{1,2}$ of (42)). We also expect the four equilibria of table I to persist, in particular the unstable star (i). However (ii)-(iv) will have $|A_{1e}| \neq |A_{2e}|$, and their type for $\sigma_r > 0$ will depend on the parameters $\mathbf{Q}$. As the linear amplifications ($\sigma_{1,2}$) and nonlinear attenuations ($K_{11}, K_{12}, K_{21}, K_{22}$) are varied in complicated ways by $\mathbf{Q}$, any combinations allowing for at least one stable equilibrium are *a priori* possible, *i.e.* only (ii) stable, only (iii) stable, only (iv) stable, or a combination of two or three of them, with different basins of attractions. In other words, we expect two types of scenarios: either that, regardless of the initial conditions, one mode only, or both modes, could reach finite equilibrium amplitude(s); or the initial conditions could decide whether one mode, or both modes would reach finite equilibrium amplitude(s).
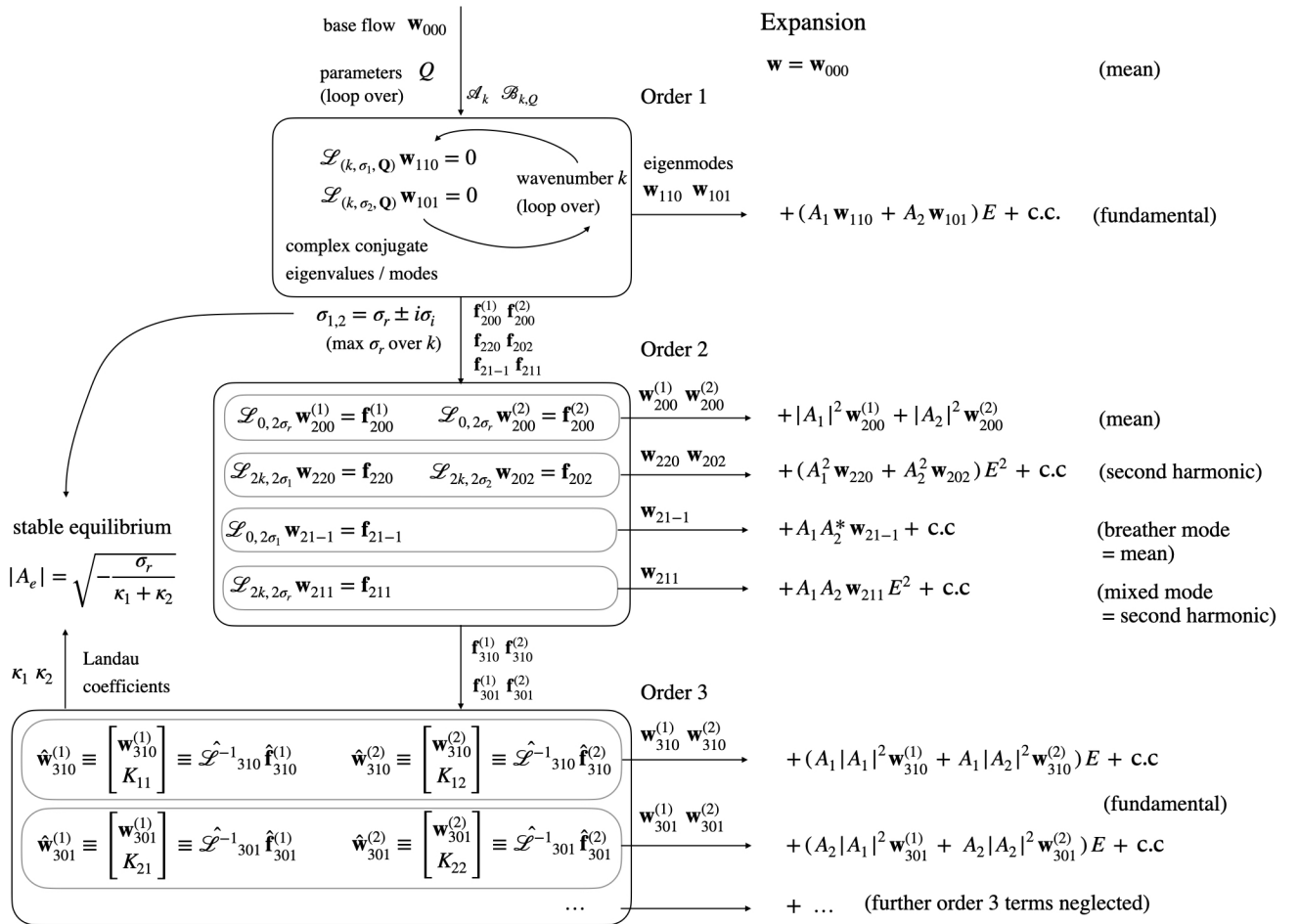
FIG. 2: Algorithm to obtain the double-mode expansion and equilibrium amplitude (summarizing § III C in the symmetric Holmboe case $E_1 = E_2 = E = e^{ikx}$).

6. Algorithm

Figure 2 summarizes the above double-mode algorithm. The key equations to solve are boxed: (9) (same eigenvalue problem as for the single-mode analysis but with complex conjugate solutions), followed by (27), (29), (31), (33), (37), (39) (matrix inversions), and row (iv) of table I.

Note that the expansion on the right-hand side of figure 2 is less general than expansion (21) in that it specifically describes the symmetric Holmboe case in which $E_1 = E_2 = E = e^{ikx}$ (since it is the case investigated in this paper, and it simplifies the figure and its interpretation). We however retained the important distinction between A_1, A_2 because for general initial conditions $A_1(t) \neq A_2(t)$, even though at the stable equilibrium $|A_{1e}| = |A_{2e}| = |A_e|$.

The numerical implementation is discussed next, and the results are discussed in §§ IV-V

D. Numerical implementation

Discretization – The problem was discretized in the vertical direction on a uniform grid of $N = 500$ points. The differential operators were discretized by second-order accurate finite differences (centered in the middle, one-sided at the boundaries). This formulation was chosen because (i) it was relatively straightforward to implement in Matlab and ran sufficiently fast on workstations for the cases investigated in this paper; (ii) it provided well-converged bifurcation diagrams and spatial structures (stencils with higher-order accuracy did

not significantly improve convergence).

Boundary conditions – The domain was set to $z \in [-3, 3]$ in an attempt to avoid finite-height effects (at the boundaries $u_{00} = \pm 0.995$ and $\rho_{00} = \pm 1.00$). The boundary conditions at $z = \pm 3$ ensure that all density and velocity perturbations cancel: $\rho = u = w = 0$. The latter two were implemented through the perturbation streamfunction ($\psi = \partial_z \psi = 0$). These boundary conditions mimick solid boundaries and proved to be the most natural and straightforward to implement (using ghost points).

IV.   RESULTS: AMPLITUDES

In this section we present our results on the weakly-nonlinear amplitudes. We start with identifying interesting locations on the linear stability boundary in § IV A, then tackle the asymptotic equilibrium amplitudes (bifurcation diagrams) in § IV B, and finally the transient dynamics (phase portraits) in § IV C.

A.   Linear stability boundary and bifurcation locations

In figure 3a we plot contours of the linear growth rate σ_r maximized over all wavenumbers k (solid lines spaced by 0.01) in the (Re, J) plane (log-log scale spanning four orders of magnitude in either dimension). We recall that the three remaining parameters (θ, Pr, R) are constant and set as in (4). The blue contours at low J represent a Kelvin-Helmholtz instability ('KH', *i.e.* a single mode with $\sigma = \sigma_r + 0i$) whereas the red contours at higher J represent a Holmboe instability ('H', *i.e.* a double mode with $\sigma = \sigma_r \pm i\sigma_i$). In the H region, we superimpose contours of the phase speed $|c| = |-\sigma_i/k| \neq 0$ (thin dashed lines spaced by 0.1). We see that both instabilities coexist in a narrow band $J \approx 0.02 - 0.05$. However, when looking at the stability boundary $\sigma_r = 0$, shown as a thick solid line, the KH to H transition occurs at $(Re, J) \approx (30, 0.02)$. In agreement with previous linear stability studies, both the KH and H growth rates increase monotonically with Re, and the KH growth rate decreases monotonically with J [29]. The KH instability appears to be bounded above by $J \approx 0.05$, corresponding to a mid-point (maximum) gradient Richardson number $Ri_{g,00}(z = 0) = JR \approx 0.25$. Futhermore, the H growth rate has an interesting non-monotonic behavior in J: at high Re, σ_r reaches a maximum at $J \approx 0.3$, a minimum at $J \approx 2$, another (weak) maximum at $J \approx 5$, etc. This causes the stability boundary to bend 'right' towards high Re between $J \approx 0.3 - 2$, to bend 'left' towards low Re between $J \approx 2 - 5$, and so on (note that values of $J \gtrsim 5$ are of lesser interest to us because rarely encountered in natural flows).

In figure 3b we plot the same stability boundary $\sigma_r = 0$, and add the wavenumber k_c at which the maximum $\max_k \sigma_r = 0$ is achieved in colour. We see that this phenomenon of non-monotonic behaviour of $\sigma_r(J)$ is associated with changes in the most unstable wavenumber. As J increases in the range $J \approx 0.3 - 2$, k also increases from ≈ 0.3 (long waves) to ≈ 3 (short waves) since the increasingly large potential energy of long waves render them more stable. However, as J further increases in the range $J \approx 2 - 5$, k takes again small values $\approx 0.5 - 1$.

This interesting linear instability behaviour allows us to identify three qualitatively different H mode couples of interest, and to pick three representative marginally-stable modes on the stability boundary for our weakly-nonlinear analysis (in red):

   1. a long-wave, weakly-stratified, slow-traveling H double-mode called H_1;

   2. a short-wave, strongly-stratified, fast-traveling H double-mode called H_2;

   3. a long-wave, strongly-stratified, fast-traveling H double-mode called H_3

We also pick a representative marginally-stable long-wave KH single mode called KH_1 (in blue). We note with interest that relatively small changes in J can drastically change the type of instability from KH_1 to H_1 or from H_2 to H_3. In the following, we will investigate weakly-nonlinear bifurcations from these four representative locations, whose 'critical' Re_c, J_c, k_c, c_c values at marginal stability ($\sigma_r = 0$) are summarized in table II.
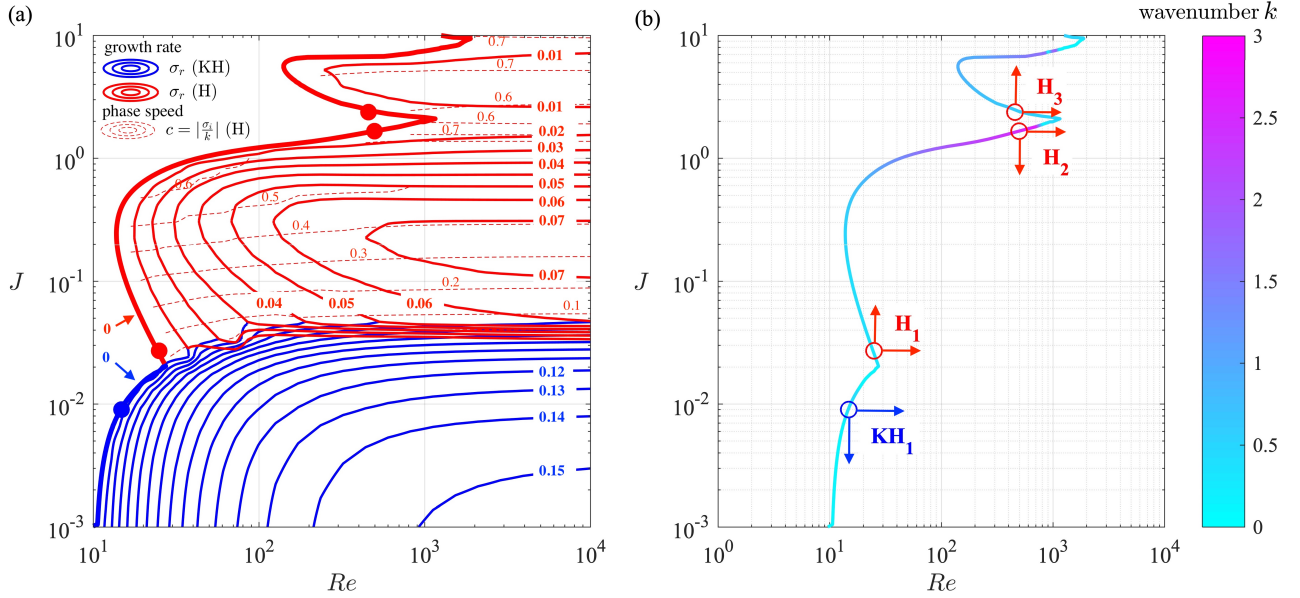
FIG. 3: Linear stability results for the base flow (2) in the (Re, J) plane of parameters as in (4). Note the log-log scale. (a) Contours of the most unstable linear growth rate σ_r maximised over k (solid) and phase speed $c = |\sigma_i/k|$ (dashed). Blue denotes Kelvin-Helmholtz instability (single mode with $c = 0$); red denotes Holmboe instability (double mode with two opposite $\pm c$). The stability boundary $\sigma_r = 0$ is shown as a thick solid line. (b) Stability boundary showing the variation of the critical wavenumber k_c (maximising $\sigma_{r,c} = 0$), as well as the four bifurcation locations and directions in (Re, J), as in (a) (coordinates given in table II).

TABLE II: Critical parameters for the four bifurcation cases considered in the remainder of the paper (one Kelvin-Helmholtz and three Holmboe instabilities). Their locations on the stability boundary are shown in figure 3.

name	Re_c	J_c	k_c	$c_c = -\sigma_{i,c}/k_c$
KH$_1$	14.8	0.0090	0.41	0
H$_1$	24.6	0.026	0.34	± 0.15
H$_2$	498	1.66	2.5	± 0.70
H$_3$	458	2.37	0.71	± 0.50

B. Bifurcation diagrams

The bifurcations diagrams were constructed using the algorithm in figure 1 for KH$_1$ and in figure 2 for H$_1$, H$_2$, H$_3$. All bifurcations were run for increasing $Re > Re_c$; however KH$_1$ and H$_2$ were run for decreasing $J < J_c$ while H$_1$ and H$_3$ were run for increasing $J > J_c$, reflecting the non-monotonic behavior of σ_r with J in the Holmboe instability. The direction of bifurcations is summarized by the arrows in figure 3b.

The results are shown in figure 4; the left column (panels a,c,e,g) show the bifurcations in Re, while the right column (panels b,d,f,h) show the bifurcations in J. The four rows correspond to the four cases in table II. Two-dimensional bifurcation diagrams in the (Re, J) plane were computed and inspected but provided little additional information compared to the one-dimensional diagrams shown here.

1. Qualitative analysis

First, focusing on the stable equilibrium amplitude $|A_e|$ curves (black thick solid), we notice that the classical supercritical pitchfork scaling $|A_e| \propto \sqrt{Re - Re_c}$ or $\sqrt{|J - J_c|}$ is rarely observed at a finite distance away from the critical point. Instead of this square root scaling, we observe 'steeper' scalings (linear, or even superlinear,
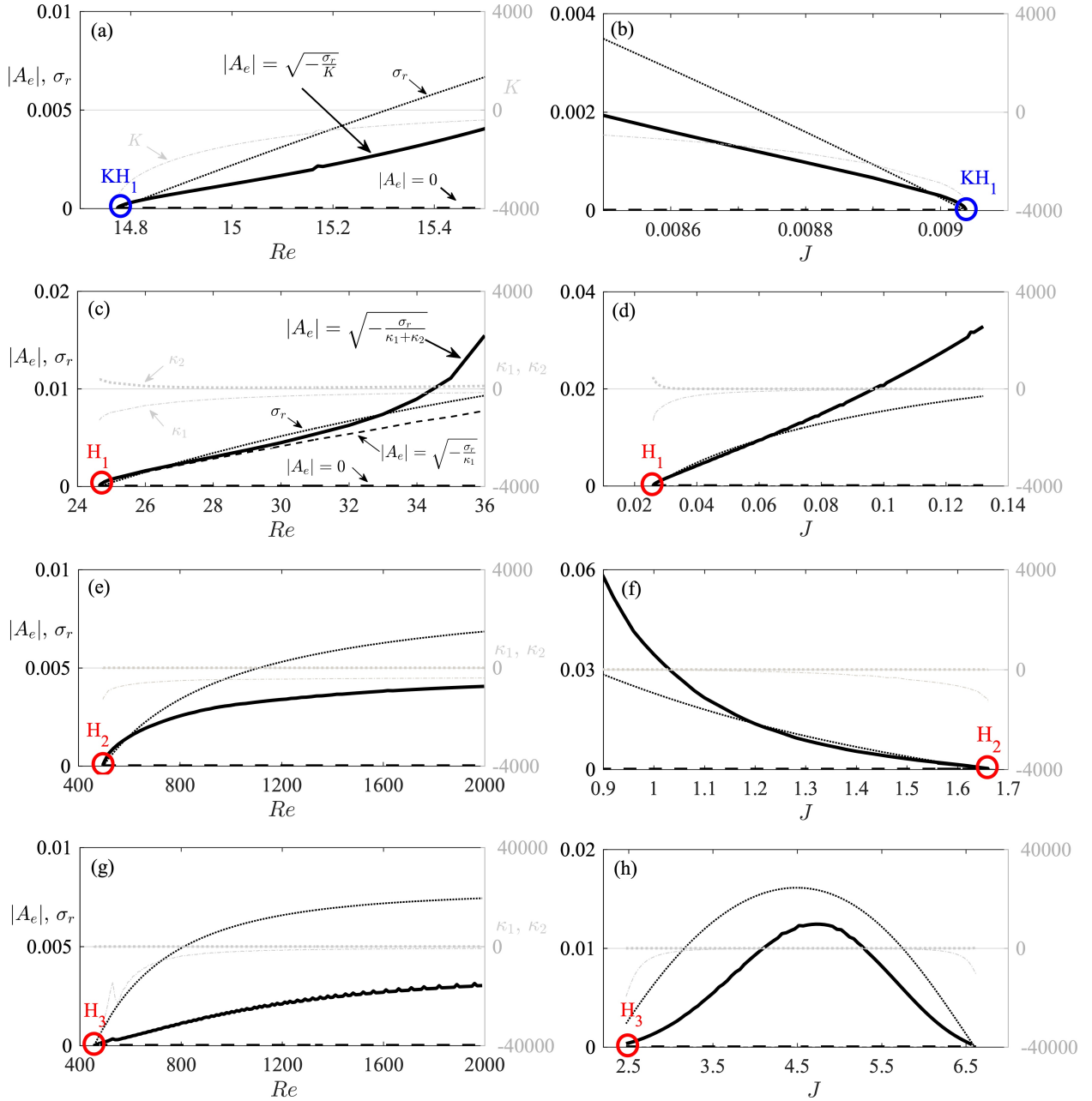
FIG. 4: Bifurcation diagrams for the four cases of table II. Left column: bifurcations in Re. Right column: bifurcations in J. We plot the unstable equilibrium amplitude $|A_e| = 0$ (in black thick dashed), stable equilibrium amplitude $|A_e|$ (in black thick solid), growth rate σ_r (in black dotted), Landau coefficients K for the single mode and κ_1, κ_2 for the double mode (in gray dash-dotted and dotted, with their own vertical axis scale in gray). Note that the double mode analysis also gives an unstable (saddle) amplitude $|A_e| \neq 0$ (in black dashed, only appreciably different from the stable amplitude in (c)).

as in panels a,b,c,d,f) and 'shallower' scalings (as in panels e,g). Surprisingly, we also observe a case in which $|A_e|$ is non-monotonic in J, reaching a peak before falling back to 0 (panel h) where it hits the stability boundary again (see figure 3b). Interestingly, we conclude that there is a large variability in the shape of these bifurcations, especially between the three H cases, and between bifurcations in Re and J.

All of these scaling behaviors in $|A_e|$ can be explained by the underlying behavior of the growth rate σ_r (black dotted line) and of the Landau coefficients K for KH_1 (gray dash-dotted line), and κ_1, κ_2 for H_1-H_3 (gray dash-dotted and dotted lines) having their own gray vertical axis on the right. The departure from the classical

pitchfork square root scaling in $|A_e|$ is explained by the fact that the scaling of σ_r is only approximately linear in panels a-c, and that K, κ_1, κ_2 are rarely constant. In particular, the Holmboe mode-specific damping coefficient $\kappa_1 < 0$ typically exhibits a sharp increase away from the critical point (*i.e.* $|\kappa_1|$ decreases) followed by a long plateau, whereas the Holmboe mode-interaction growth coefficient $\kappa_2 > 0$ typically remains relatively small $|\kappa_2| \ll |\kappa_1|$. As a consequence, the unstable (saddle) equilibrium amplitude (black dashed line) is generally indistinguishable from the stable (relevant) equilibrium amplitude, except in panel c where both are visible (see table I for a reminder).

2. *Quantitative analysis*

Second, focusing on the numerical values in $|A_e|$, the different axis limits highlight differences among all panels. Although our amplitude expansion allows us *a priori* to compute bifurcations at any arbitrary distance away from the critical point, we imposed strict 'stopping criteria' in order to show results most likely to be mathematically valid and physically sensible. Our primary criterion was that the global energy of the perturbation $(1/2)||\mathbf{w} - \mathbf{w}_{00}||^2_{\mathscr{M}}$ should not exceed 1% of that of the base flow $(1/2)||\mathbf{w}_{00}||^2_{\mathscr{M}}$ (computed using the kinetic + scalar energy norm, where $\mathscr{M}$ is defined in appendix C). This conservative criterion is consistent with the fully-nonlinear Kelvin-Helmholtz simulations of [30] who reported that 'nonlinear effects become important' at a relative energy of 0.75%. This criterion was only limiting in the H diagrams of figure 4c,d,f. Our secondary criterion was that the modulus of the perturbation density $|\rho - \rho_{00}|(z)$ should not locally exceed 0.2 anywhere in the domain (*i.e.* 20% of the maximum $|\rho_{00}|$). Although rather arbitrary, this criterion was intended to reject any clearly unphysical density perturbations. This criterion was limiting in the two KH diagrams of figure 4a,b where $|\rho - \rho_{00}|$ peaked at the interface despite contributing little scalar energy due to the low $J \approx 0.09$. Finally, when neither of these criteria was limiting, the bifurcation diagrams were stopped either because the distance from the critical point was judged excessive (at a rather arbitrary $Re = 2000$ in figure 4e,g), or because $|A_e|$ fell back to 0 (at $J = 6.5$ in figure 4h).

These stopping criteria yield 'final' values of $|A_e|$ between a minimum of 0.002 (panel b, limited by a local perturbation density of 0.2) and a maximum of 0.06 (panel f, limited by a global perturbation/base flow energy of 1%). Overall KH$_1$ reach their final $|A_e|$ much more 'rapidly' than any H in terms of relative distance to the critical point $(Re - Re_c)/Re_c$ and $|J - J_c|/J_c$. It is particularly interesting to compare KH$_1$ and H$_1$ (panels a-d), which are so close in parameter space (Re, J), but so different in weakly-nonlinear behaviour. The 'faster' growth of $|A_e|$ in KH$_1$ than in H$_1$ (again in terms of relative distance to the critical point) is no doubt primarily caused by a higher linear σ_r, but the latter is counter-balanced by a larger Landau damping constant $|K| \gg |\kappa_1|$. Among H (panels c-h) the 'slower' growth of $|A_e|$ at increasing J (*i.e.* H$_3$ is generally 'slower' than H$_2$, and H$_2$ is 'slower' than H$_1$) not only results from generally lower σ_r, but also from higher damping $|\kappa_1|$. It is particularly interesting to compare H$_2$ and H$_3$, which are so close in parameter space, but have very different $|\kappa_1|$ near the critical point (the gray right axis limits in panels g,h are ten times larger than in the other panels). Overall, this suggests that weakly-stratified, low-Re Holmboe waves will reach appreciable amplitudes much more 'rapidly' than strongly-stratified, high-Re Holmboe waves.

In most panels, the distance away from the critical point is larger than is typically 'allowed' in weakly-nonlinear analyses. However, as explained in § III A, our amplitude expansion is different from a multiscale expansion in that its validity is not restricted to a small distance away from the critical point. Instead, the validity of our diagrams is guaranteed *a posteriori* as long as $|A_e|$ remains small enough for our truncation of the Stuart-Landau series (15), (22) to accurately approximate the full series $(1/|A|)d|A|/dt$. Although it appears to be the case, we cannot exclude that the next term in the series $(\propto |A|^4)$ might be multiplied by a very large second Landau coefficient, rendering it non-negligible and effectively reducing the radius of convergence of the series below what we assumed in figure 4. Such a scenario would be interesting; however, a tedious amplitude expansion up to order 5 would be required to obtain the second Landau coefficient and verify it.

C. **Phase portraits**

We now turn our attention to the transient dynamics of weakly-nonlinear Holmboe waves in the phase space $(|A_1|, |A_2|)$, as introduced in § III C 5 (recall the shorthand notation $A_1 = A_{110}, A_2 = A_{101}$). Our results of $\sigma_r, \kappa_1, \kappa_2$ allow us to plot phase portraits of the two-dimensional Stuart-Landau dynamical system (22) for a given couple (Re, J). These phase portraits describe the unsteady growth of the amplitude of each mode (from
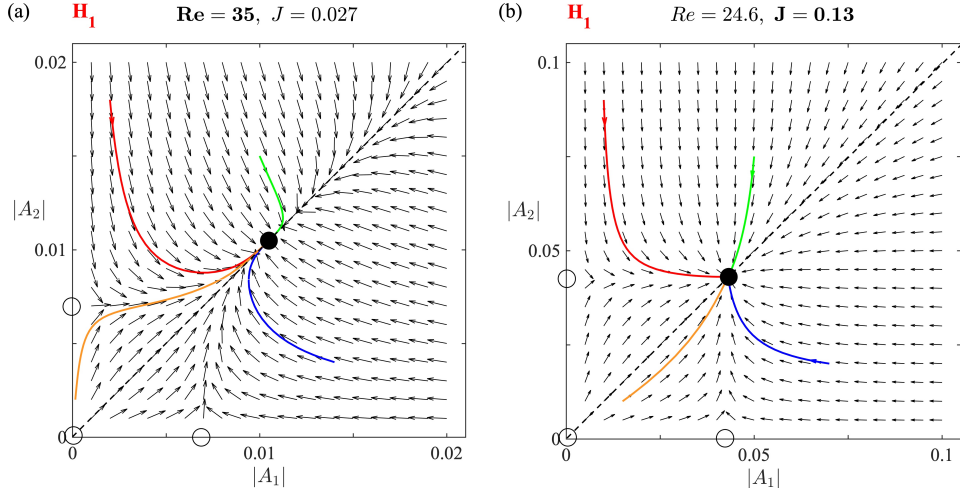
FIG. 5: Phase portraits showing the transient dynamics of weakly-nonlinear Holmboe waves for location H_1 in (a) Re and (b) J (see figure 4c-d). In addition to the tangent arrows, we plot the three unstable fixed points (empty circles), the stable fixed point $|A_1| = |A_2| = |A_e|$ (full circle) and four example trajectories.

arbitrary initial conditions) and asymptotic saturation to the stable equilibrium $(|A_e|, |A_e|)$ (whose value is given by the previous bifurcation diagrams).

The results are shown in figure 5 for case H_1 only, since the results for H_2 and H_3 are similar and are not shown for conciseness. In panel a (resp. panel b) we show the phase portrait near the 'final' bifurcation location $Re = 35$ (resp. $J = 0.13$). These portraits have a mirror symmetry with respect to the unit line $|A_1| = |A_2|$ (dashed line), as expected in symmetric Holmboe waves. Any slight asymmetry in the location of the base density profile ρ_{00} with respect to the velocity profile u_{00} would break this symmetry and result in more intricate (and interesting) transient dynamics and fixed points stability, as explained in § III C 5.

These portraits illustrate the fact that complex conjugate symmetric Holmboe modes can transiently have very different amplitudes, and how they converge to the equilibrium stable node. In most cases, including case H_1 in J (panel b), this convergence is monotonic, *i.e.* $|A_1(t)|$ and $|A_2(t)|$ either grow or decay monotonically to equilibrium. However, in the exceptional case of H_1 in Re (panel a), this convergence is non-monotonic, *i.e.* $|A_1(t)|$ and $|A_2(t)|$ can transiently grow above or decay below the equilibrium value. This is due to the fact that the two saddles $|A_e| = \sqrt{-\sigma_r/\kappa_1}$ (empty circles on the axes) are located below the stable node $|A_e| = \sqrt{-\sigma_r/(\kappa_1 + \kappa_2)}$ (full circle), a fact that we indeed noted as exceptional in case H_1 in Re (figure 4c). These non-monotonic transient dynamics are ultimately caused by a mode-mode interaction coefficient κ_2 which is non-negligible compared to the mode-specific coefficient κ_1. Why this is observed only in the long-wave, weakly-stratified H_1 mode, and only at supercritical Re (not J), remains an open question.

V. RESULTS: FLOW STRUCTURES

In this section we present our results on the weakly-nonlinear flow structures. We start with the vertical (z) profiles of each term in the amplitude expansion in § V A, before turning to the planar (x, z) contours in § V B.

A. Vertical structures in z

1. Kelvin-Helmholtz case KH_1

In figure 6 we deconstruct the single-mode perturbation of (13) and figure 1 in case KH_1 near the final bifurcation locations in $Re > Re_c$ (top row) and in $J < J_c$ (bottom row). To do so, we plot the vertical profiles of the modulus of (from left to right) the order 1 term $|A_e||\mathbf{w}_{11}|$, order 2 terms $|A_e|^2|\mathbf{w}_{20}|, |A_e|^2|\mathbf{w}_{22}|$, and order 3 terms $|A_e|^3|\mathbf{w}_{31}|, |A_e|^3|\mathbf{w}_{33}|$. To provide a complete picture, we examine the streamfunction $|\psi|$

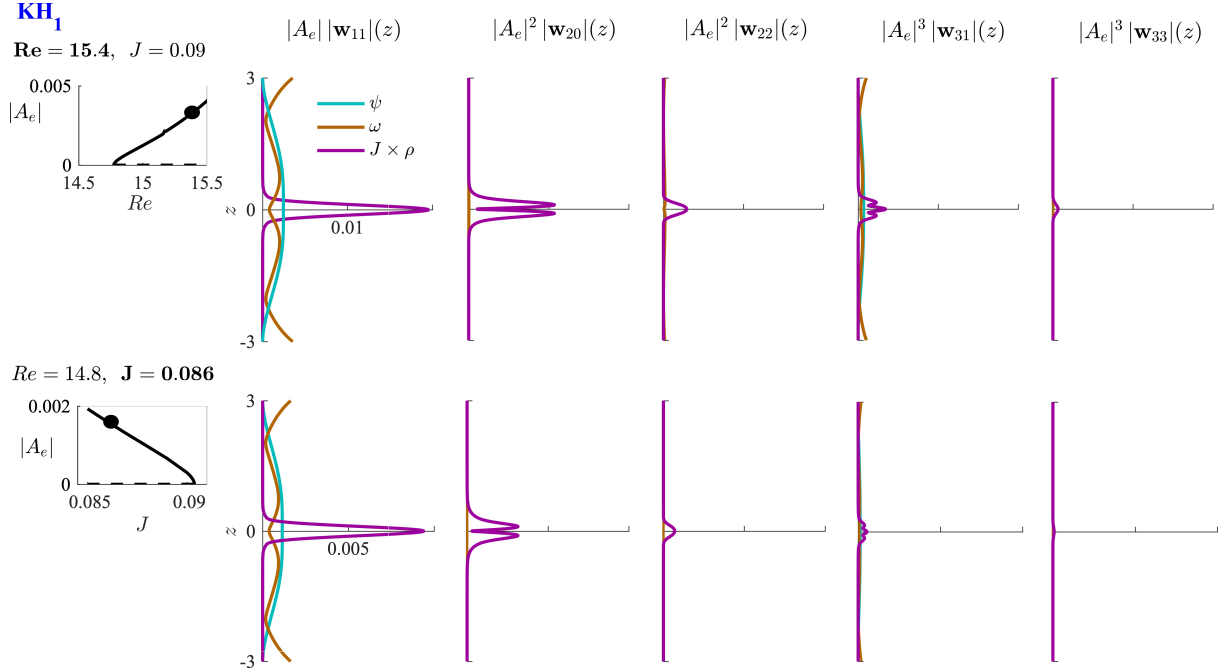FIG. 6: Vertical structure of a deconstructed weakly-nonlinear Kelvin-Helmholtz perturbation KH_1, away from the critical point in Re (top row) and J (bottom row). From left to right: inset showing the location on the bifurcation diagram (taken from figure 4a,b); order 1 fundamental mode; order 2 mean and second harmonic modes; and order 3 fundamental and third harmonic modes (see expansion in (13) and figure 1). Axis limits are identical across a given row.

(in cyan, a proxy for the vertical velocity $|w| \propto |\partial_x \psi| \approx k|\psi|$), the vorticity $|\omega| = |\nabla^2 \psi|$ (in orange), and the density $|\rho|$ (in purple). The latter is multiplied by J in order to more accurately reflect the importance of density in this weakly-stratified case. Although the Kelvin-Helmholtz case is not the primary focus of this paper, we believe that figure 6 provides a useful introduction and basis for the more complicated Holmboe cases in the next section.

First, comparing both rows, we notice that the bifurcations in Re and J yield very similar vertical profiles (despite a factor two in the amplitude). As expected, all profiles are perfectly symmetric about $z = 0$.

Second, examining either row column by column, we notice that the order 1 fundamental $|A_e||\mathbf{w}_{11}|$ is by far dominant, except in the density field. The dominant higher-order term chiefly responsible for nonlinear saturation appears to be the order 2 feedback on the mean density $|A_e|^2|\rho_{20}|$, which has a distinct double peak on either side of the density interface, in contrast with the order 1 fundamental which has a single peak. The order 2 second harmonic $|\rho_{22}|$, the order 3 first harmonic $|\rho_{31}|$, and the order 3 third harmonic $|\rho_{33}|$ have yet different and interesting structures localized at the interface, but are comparatively small.

2. Holmboe cases H_1, H_2, H_3

In figure 7 we deconstruct the double-mode perturbations of (21) and figure 2 in cases H_1, H_2, H_3 (top to bottom row), both in Re and J (see bold parameters and bifurcation diagram insets in the leftmost column). The figure is designed much like the previous figure 6; in particular all modes are plotted already multiplied by their respective amplitude ($|A_e|$, $|A_e|^2$, $|A_e|^3$). In this double-mode analysis, we only plot the seven terms that result from mode 1 (a.k.a. mode 110) and a combination of modes 1 and 2. The remaining five terms result from the counter-propagating mode 2 alone (a.k.a. mode 101); they can thus be deduced from their respective counterpart by the symmetry relation (10), and would provide no additional information (these are $\mathbf{w}_{101}$, $\mathbf{w}_{200}^{(2)}$, $\mathbf{w}_{202}$, $\mathbf{w}_{301}^{(1)}$, $\mathbf{w}_{301}^{(2)}$).

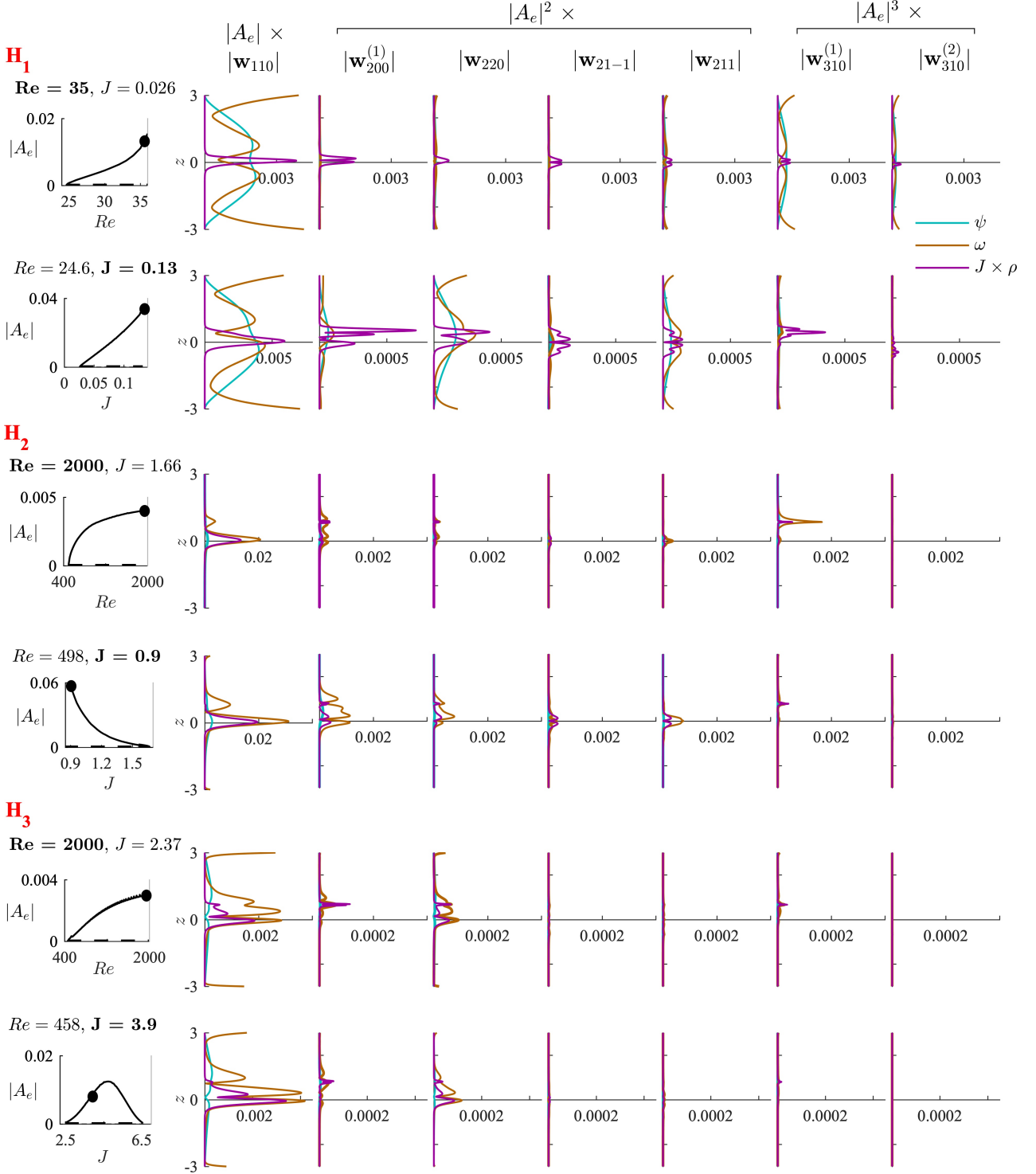First, by surveying the relative magnitude of each term, we note that in all rows except the top row, the

FIG. 7: Vertical structure of deconstructed weakly-nonlinear Holmboe perturbations H_1, H_2, H_3, away from the critical point in Re and J (top to bottom). From left to right: inset showing the location on the bifurcation diagram (taken from figure 4c-h); order 1 fundamental mode; order 2 mean, second harmonic, breather and mixed modes; and order 3 fundamental modes (see expansion in (21) and figure 2). The remaining five terms resulting from mode 2 alone can be deduced by (10).

order 2 and order 3 terms are plotted on a horizontal scale that is ten times smaller than the order 1 term for visualisation purposes. As a consequence, the general appearance of the total weakly-nonlinear perturbation (sum of all these terms) should only be a minor distortion of the order 1 fundamental mode $\mathbf{w}_{110}$.

Second, by focusing on this mode $\mathbf{w}_{110}$ (first column), we find that for a given case (H_1, H_2, or H_3) this mode remains fairly similar away from the critical point, whether the bifurcation is in Re or J. However, we find clear differences in $\mathbf{w}_{110}$ across the three H cases, both in the structure of the individual ψ, ω, ρ (broad or localised character, shape of the peaks) and in their relative magnitude. In other words, the structure of Holmboe waves shows much variation in the (Re, J, k) space (however this is a linear phenomenon).

Third, by looking for the dominant higher-order nonlinear terms (order 2 and 3), we find again differences across the three H cases, but similarities between their respective bifurcations in Re or J. In H_1, nearly all order 2 and order 3 terms contribute significantly, albeit with very different structures. In H_2, most terms remain significant, and only a couple become insignificant. In H_3, which we remember is so close to H_2 in parameter space, only two order 2 terms remain significant: the distortion of the mean flow $\mathbf{w}_{200}^{(1)}$ (caused by self-interaction of $\mathbf{w}_{110}$ with its implicit complex conjugate) and the second harmonic $\mathbf{w}_{220}$ (caused by self-interaction of $\mathbf{w}_{101}$). The former is highly localised well above the density interface, while the latter affect the shear layer more globally.

Interestingly, we note in case H_2 in Re the rather unexpected dominance of the order 3 term $\mathbf{w}_{310}^{(1)}$ (caused by the interaction of the second harmonic $\mathbf{w}_{220}$ with the complex conjugate of $\mathbf{w}_{110}$ and of the mean flow distortion $\mathbf{w}_{200}^{(1)}$ with $\mathbf{w}_{110}$). This could be an artefact caused by an excessively large distance away from the critical point; however we must stress that the amplitude remains very small $|A_e| \approx 0.003$, and corresponds here to a global perturbation energy of $0.0012\,\%$ of the mean flow (well below our $1\,\%$ stopping criterion). However, we will not delve further on case-by-case analyses of order 3 terms since Appendix A 2 makes it clear that they are exceedingly difficult to interpret physically.

However, our result demonstrate that in parallel stratified shear flows the mean flow distortion $\mathbf{w}_{200}^{(1)}$ does not appear to be generally and overwhelmingly dominant, in contrast with the assumptions and results of the 'self-consistent mean flow analysis' of Mantič-Lugo, Arratia & Gallaire [33] who tackled vortex shedding in the wake of a cylinder.

B. Planar structures in (x, z)

1. Reconstructed perturbations

To complement our previous deconstructions and analyses of vertical structures, we now turn to the reconstructions (sum) of perturbations and analyses of their full two-dimensional, planar structures in (x, z) (with phase information). In figure 8 we plot, for all four cases (KH$_1$, H_1, H_2, H_3), the reconstructed expansion corresponding to figures 6-7 (thick solid contours). We superimpose the order 1 fundamental mode (or 'linear' mode, thin dashed contours) in order to assess the nonlinear distortion caused by order 2 and order 3 terms. For each field, we plot a single wavelength along x, and a single couple of contours of opposite values (e.g. ± 0.003, ± 0.001 etc) near the maximum values in order to faithfully represent the dominant shape of the signal.

Two further technical details are worth mentioning. First, we plot these contours at a single time (snapshot) when the complex amplitude is real $A_e = |A_e|\mathrm{e}^{i0}$, i.e. has zero phase. We do this without loss of generality since the phase varies linearly in time and does not saturate to a fixed point equilibrium like the modulus $|A_e|$. Second, as in figure 7, we only plot the terms corresponding to mode 1 and the stationary (standing wave) combinations of mode 1 and 2; the remaining five terms resulting from the counter-propagating mode 2 alone (deduced by symmetry) are not added. The reason is that the total wave field resulting from the superposition of two counter-propagating Holmboe modes can take very different shapes based on their relative phase shift. By avoiding an arbitrary choice of phase shift and mode superposition, we facilitate the present comparison of the nonlinear effects on a single mode.

To begin with, a quick comparison between the thick solid and thin dashed contours in all panels reveals that the reconstructed perturbation is almost indistinguishable from the linear mode. In other words, the effects of higher-order modes, although sufficient to saturate the growth of the linear mode to an finite-amplitude equilibrium, are not sufficient to visibly alter its planar structure. This is of course a consequence of the
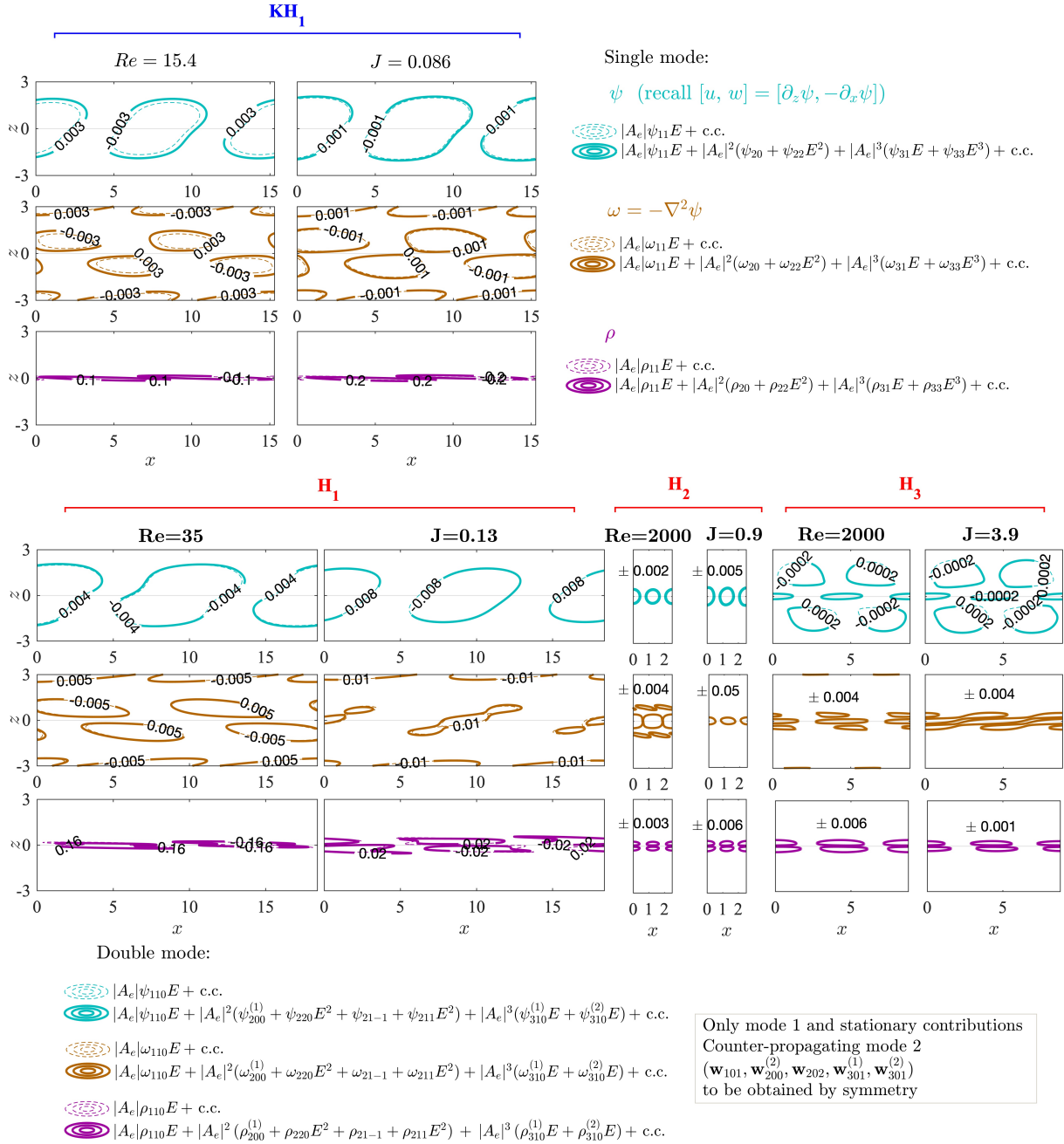
FIG. 8: Planar structure of reconstructed weakly-nonlinear expansions in the Kelvin-Helmholtz case (KH$_1$, top half) and Holmboe cases (H$_1$, H$_2$, H$_3$, bottom half). The linear mode is superimposed for comparison (dashed contours). The value of each pair of contours is chosen near the maximum value to highlight the main signal. The bifurcation locations are given by the bold parameter Re or J, and correspond to those in figures 6-7. In the H cases, we only plot harmonics of mode 1 and mean modes resulting from mode 1 and 2 (avoiding the superposition of counter-propagating mode 2 harmonics, which have a known symmetry).

relatively small 'final' amplitudes $|A_e|$, which result from our stopping criteria. These stopping criteria were chosen as 'reasonable' in order for the expansion to remain valid and sensible, but they have an inherent degree of arbitrariness. Although it would be possible to 'push' some of these bifurcations to larger $|A_e|$ and find structures with stronger nonlinear distortion, the question of their validity must always be kept in mind.

Having established that the linear modes are excellent approximations of all 'reasonable' weakly-nonlinear expansions, we briefly comment on them, especially on the differences between H cases, as briefly noted in
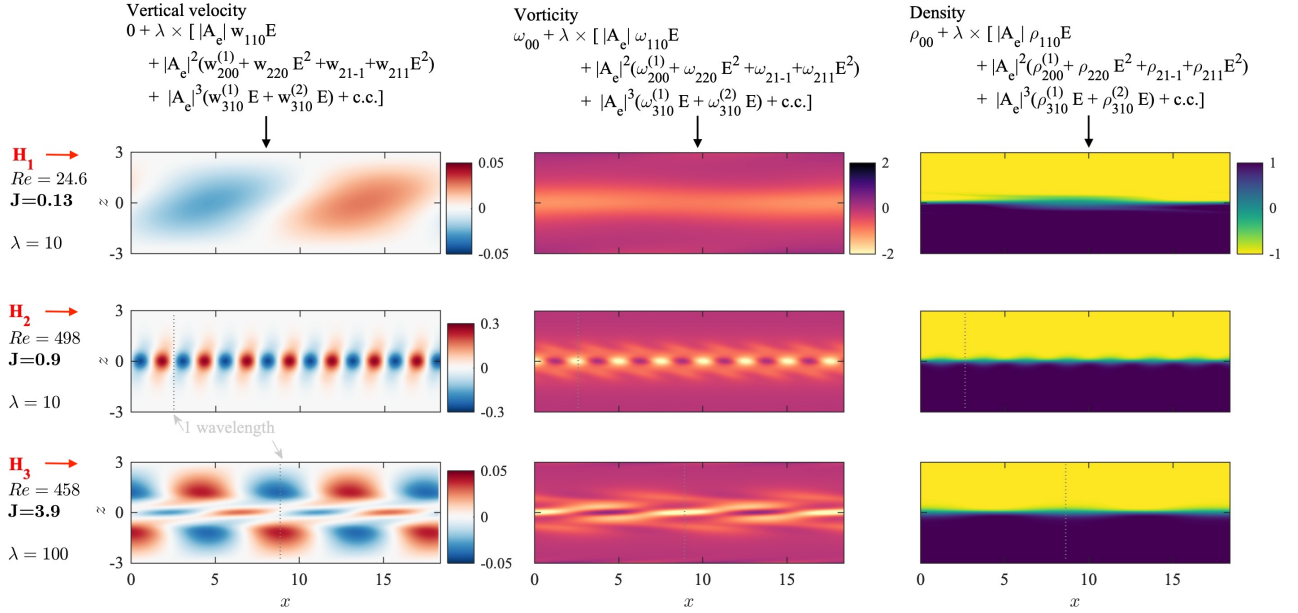
FIG. 9: Visualizations of the total flow in cases H_1 (top row), H_2 (middle row), H_3 (bottom row). The total vertical velocity w (left column), spanwise vorticity ω (middle column), and density (right column) are obtained by adding to the base flow ($w_{00} = 0, \omega_{00} = -\operatorname{sech}^2 z, \rho_{00} = -\tanh 5z$) the reconstructed perturbation of figure 8 magnified by a factor $\lambda = 10$ or 100 for easier visualization. Colorbars are identical in the middle and right column.

figure 7. First, the linear modes have different structures when computed away from the critical point in Re or J (compare the two columns of either H_1, H_2, H_3). In other words, nonlinearities essentially tell us how far away from the critical point the expansion can be computed, and therefore allow us to find the structure of the linear mode at this distance, which can differ from the critical mode. Second, the linear modes themselves have different structures across the three H cases, beyond the obvious differences in wavelengths $2\pi/k$ (long wave *vs* short wave). The weakly-stratified, slow-traveling Holmboe case H_1 is very similar to the Kelvin-Helmholtz case KH_1, and very different from the two highly-stratified fast-traveling Holmboe cases H_2, H_3. In the latter two, the vorticity perturbation is more localized at the interface, and the density has a double perturbation above and below the interface which are almost perfectly in phase (this phase information was not contained in figure 7).

2. Reconstructed total flow

We plot in figure 9 visualizations of the total weakly-nonlinear Holmboe flow fields at equilibrium, including the reconstructed expansion (the 'perturbation') and the base flow. We plot the vertical velocity $w = -\partial_x \psi$, vorticity ω, and density ρ with a streamwise extent equal to one H_1 wavelength in all panels (which corresponds to multiple wavelengths in H_2, H_3). This visualization would be typical of experimental measurements using particle image velocimetry (PIV) and planar laser induced fluorescence (PLIF) as done in Lefauve [11] (§ 3.2) and Lefauve *et al.* [12] (see their figure 8). However, since the perturbations are too small to be easily visualized here, we artificially magnified them by a factor $\lambda = 10$ in H_1–H_2 and $\lambda = 100$ in H_3 (making them 10 or 100 times more dramatic). For conciseness, we only show results for the bifurcations in J (not Re, see parameter in bold on the left).

This figure gives us yet another view of the differences in structure between the three Holmboe cases, which as we now know, is primarily due to their linear mode. We note the particularly strong w signal in H_2 (middle left panel, having larger colorbar limits) relative to the other signals (in particular the ρ signals are all comparable). We also note the strong and characteristically different ω signals in H_2 and H_3. However, it must be remembered that the perturbations have been amplified by factors of 10 and 100 respectively, in order to reach a level typical of some laboratory flows.

C. Saturation energetics

To conclude this section, we comment on the mechanism responsible for nonlinear saturation from an energetics point of view. Consider the mean and perturbation kinetic energies,

$$\bar{K}(z) \equiv \frac{1}{2}\bar{\boldsymbol{u}} \cdot \bar{\boldsymbol{u}} \quad \text{and} \quad K'(x,z,t) \equiv \frac{1}{2}\boldsymbol{u}' \cdot \boldsymbol{u}', \tag{43}$$

respectively associated with the mean flow $\bar{\boldsymbol{u}} \equiv \langle \boldsymbol{u} \rangle_{x,t}$ (averaged in the periodic streamwise direction and time) and the (x,t)-periodic perturbations away from it $\boldsymbol{u}' \equiv \boldsymbol{u} - \bar{\boldsymbol{u}}$. By analogy, we also consider the mean and perturbation scalar variances:

$$\bar{K}_\rho(z) \equiv \frac{J}{2}\bar{\rho}^2 \quad \text{and} \quad K'_\rho(x,z,t) \equiv \frac{J}{2}\rho'^2, \tag{44}$$

with $\bar{\rho} \equiv \langle \rho \rangle_{x,t}$, $\rho' \equiv \rho - \bar{\rho}$. The temporal evolution equations for each energy or variance is deduced from (1), and when averaged over x and t, give the following budgets:

$$\overline{\partial_t K} = -P + F - \bar{D} \quad (\bar{K} \text{ budget}), \tag{45a}$$

$$\overline{\partial_t K'} = +P - B - D \quad (K' \text{ budget}), \tag{45b}$$

$$\overline{\partial_t K_\rho} = -P_\rho + F_\rho - \bar{\chi} \quad (\bar{K}_\rho \text{ budget}), \tag{45c}$$

$$\overline{\partial_t K'_\rho} = +P_\rho - \chi \quad (K'_\rho \text{ budget}). \tag{45d}$$

The fluxes are: the production terms $P \equiv -\overline{u'w'}\partial_z \bar{u}$, $P_\rho \equiv -J\overline{w'\rho'}\partial_z\bar{\rho}$; the forcing terms F, F_ρ (see equation (3)); the buoyancy flux $B \equiv J\overline{w'\rho'}$ (related to P_ρ); and finally the dissipation terms $\bar{D} \equiv (2/Re)\bar{\mathsf{s}}_{ij}\bar{\mathsf{s}}_{ij}$, $D \equiv (2/Re)\overline{\mathsf{s}'_{ij}\mathsf{s}'_{ij}}$ (s being the strain rate tensor), $\bar{\chi} \equiv J/(Re\,Pr)\partial_{x_i}\bar{\rho}\partial_{x_i}\bar{\rho}$, and $\chi \equiv J/(Re\,Pr)\overline{\partial_{x_i}\rho'\partial_{x_i}\rho'}$ (summing over repeated indices).

During the unsteady growth of the instability, the average of any quantity ϕ over a period T (taken as the first harmonic) is $\overline{\partial_t \phi}(t) = (1/T)(\langle \phi \rangle_x(t+T) - \langle \phi \rangle_x(t)) \neq 0$. As a result, the mean budgets (45a), (45c) do not exactly cancel, because the initial base flow $\mathbf{w}_{000}$ is being modified by the mean flow feedback at order 2 (which we recall are $|A_1|^2\mathbf{w}_{200}^{(1)}$, $|A_2|^2\mathbf{w}_{200}^{(2)}$ and $A_1 A_2^*\mathbf{w}_{21-1}$+c.c.). In the meantime, the perturbation budgets (45b), (45d) also vary from period to period, since the essence of a linear instability ($\sigma_r > 0$) is precisely to transfer enough mean energy to perturbation energy through P such that $P - B - D > 0$ (indeed when computed using only the linear mode $\mathbf{w}_{110}, \mathbf{w}_{101}$, $P - B - D$ is proportional to σ_r). As the amplitudes A_1, A_2 increase and further harmonics are generated, the nonlinear saturation mechanism observed in this paper (typical of supercritical pitchforks) corresponds to the gradual modification of all fluxes in (45) by order 2 and 3 terms until a stable equilibrium is reached and all budgets cancel $\overline{\partial_t K} = \overline{\partial_t K'} = \overline{\partial_t K_\rho} = \overline{\partial_t K'_\rho} = 0$.

A more detailed and physically-based understanding of weakly-nonlinear Holmboe waves would require the computation and comparison of all fluxes in (45) at equilibrium, using the the total flow expansion (21) (having four mean flow contributions and nine periodic contributions, not including complex conjugates). An even more detailed investigation of the role of individual higher order terms in the vertical structure of the flow, *e.g.* causing the local distortion of the mean shear layer or the sharpening/broadening of the mean density interface, would require the investigation of all products of periodic contributions, especially in the crucial P, P_ρ, B fluxes, which are each composed of $9 + 8 + \ldots + 1 = 45$ dyadic products (where the average of each dyad is given by $\overline{\{a(z)e^{in_a k(x-ct)} + \text{c.c.}\}\{b(z)e^{in_b k(x-ct)} + \text{c.c.}\}} = a^* b + a b^*$ over a fundamental wavelength $2\pi/k$ and period $2\pi/(kc)$). Although *a priori* valuable, this study is beyond the scope of this paper.

VI. CONCLUSIONS

A. Summary

In this paper we tackled the weakly-nonlinear temporal stability properties of parallel shear flows that are stably-stratified in z (see equation (2)). We focused on Holmboe waves, comparing them in passing to the related Kelvin-Helmholtz waves, and investigated separately the role of two bifurcation parameters, the Reynolds number Re and bulk Richardson number J (equation (4)).

We developed rigorous weakly-nonlinear amplitude expansions to study the evolution of two-dimensional perturbations having a normal mode in x (periodic), and an inhomogeneous structure in z. Simply speaking, the nonlinearities in equation (3) affect the linear eigenmode (order 1 in amplitude) and excite the growth of order 2 modes (mean flow distortions and second harmonics). Further nonlinear interactions between the order 1 and order 2 modes excite order 3 modes, which eventually provide negative feedback on the exponential growth of the amplitude and stabilize it to a finite value (Stuart-Landau equations (15), (22)). The derivation takes two distinct forms in the case of a single unstable mode (Kelvin-Helmholtz instability, see expansion (13)), or in the case of a couple of complex conjugate modes (counter-propagating symmetric Holmboe instability, see expansion (21)). By carefully solving for these higher-order modes (see hierarchy in Appendix A) we proposed a single-mode algorithm (figure 1) and a double-mode algorithm (figure 2) to calculate the stable equilibrium amplitude $|A_e|$ away from the critical point where the flow first becomes linearly unstable (supercritical bifurcation).

After studying the linear stability of our system (figure 3a), we applied our weakly-nonlinear algorithms at four qualitatively distinct locations on the stability boundary (figure $3b$ and table II). We selected a low-Re, long-wave, weakly-stratified Holmboe case (named H_1, supercritical for increasing J), and two shorter-wave, strongly-stratified Holmboe cases (H_2 and H_3, supercritical for decreasing and increasing J, respectively). For comparison, we also selected a Kelvin-Helmholtz case (KH_1) very near H_1.

Our bifurcation diagrams (figure 4) showed the steady-state $|A_e|(Re, J)$ as well as the underlying linear growth rate σ_r and Landau coefficients. They revealed a variety of behaviors that are richer than the classical supercritical pitchfork typical of other (multiscale) expansions in the literature. The KH case and the three H cases all have different branches, both qualitatively in their scaling law and quantitatively in their 'final' amplitude, the latter being set by stopping criteria (capping the global perturbation energy, the local values of perturbations, or the distance away from the critical point). We then illustrated the transient dynamics of the amplitudes of the counter-propagating (double-mode) Holmboe waves with phase portraits (figure 5). This revealed that, in some rare cases, one of the two modes can transiently growth above (or decay below) its long-time equilibrium amplitude (here only in H_1 when bifurcating in Re but not in J).

Finally, we investigated the spatial structures of these weakly-nonlinear expansions at equilibrium. First, the vertical (z) structures of the deconstructed expansions (figures 6-7 showing a breakdown of the modulus of modes present at order 1, 2, 3) revealed differences across all eight cases (KH_1, H_1, H_2, H_3 when bifurcating in Re and J). Not only do they have different linear (order 1) modes, but also different higher-order (order 2 and 3) modes, and therefore, different weakly-nonlinear saturation mechanisms underlying the previous bifurcation diagrams. Although the order 2 distortion of the mean flow and the order 2 second harmonic are generally the dominant higher-order terms, in some cases other terms are significant and possess highly-localized vorticity or density structures. Second, the planar (x, z) structures of the reconstructed perturbation expansions (figure 8 showing the sum of all modes with phase information) highlighted the very weak and barely-noticeable distortions caused by higher-order modes, and gave more detailed view of the differences in order 1 modes (*e.g.* the relative magnitudes of w, the single- *vs* double-peaked ρ and its relative phase shifts, the interfacial localization of ω). Visualizations of the total reconstructed flow field (figure 9, adding the base flow) revealed the (largely linear) finite-amplitude signature of Holmboe waves as they would be observed in experiments, while highlighting their small equilibrium amplitude $|A_e|$ (the perturbation had to be artificially amplified to be clearly visible). Third, we outlined the basic energy mechanisms responsible for nonlinear saturation, and emphasized the challenges of a detailed physical understanding, which remain an open question.

Next, we discuss some limitations of these results and some possible future directions for the study of the nonlinear Holmboe dynamical system.

B. Limitations and future directions

The 'final' equilibrium amplitudes $|A_e|$ shown in our bifurcation diagrams and spatial structures are limited by the absence of a clear-cut, unambiguous criterion guaranteeing the validity of our expansions. In other words, how far away from the critical point can we 'push' the weakly-nonlinear analysis?

On the one hand, the experiments and linear stability analysis of Lefauve *et al.* [12] suggest that we might be allowed to 'push' it much further away from what we have done in the present paper. Their measurements

of finite-amplitude Holmboe waves revealed much larger perturbations (comparable to the visualization of figure 9 in which $|A_e|$ was amplified by a factor 10 to 100), which nevertheless agreed remarkably well with their most unstable linear mode (computed on the mean flow). Thus, even at larger $|A_e|$, nonlinear modes might still only very weakly distort the linear mode, and might still be well described by a weakly-nonlinear analysis (although we need to appreciate that their linear mode was computed not on a perfectly steady *base* flow but on the measured *mean* flow, which is already affected by nonlinear modes).

On the other hand, theoretical arguments and numerical studies warn against pushing the weakly-nonlinear analysis too far. First, our implicit assumption throughout the weakly-nonlinear analysis that the linear mode has a single wavenumber k (maximizing σ_r) becomes increasingly inaccurate away from the critical point, where we have instead a whole continuous band of unstable wavenumbers (clear in the dispersion relation figure 6a of [12]). Second, a proper assessment of the validity of our truncated Landau series would require the computation of second Landau coefficients, and therefore, extending our perturbation expansion to order 5 (not a trivial step as becomes clear in Appendix A). However, this course of action is discouraged by conventional wisdom because higher Landau coefficients tend to be very large, reducing the radius of convergence of the series (see [23] and the recent results of [34, 35]).

The above discussion pleads in favour of a fully-nonlinear analysis. DNSs of finite-amplitude Holmboe waves with periodic boundary conditions in x have long been performed, but not yet with the specific aim of systematically finding the bifurcation diagram $|A_e|(Re, J)$ under supercritical conditions (this requires, in particular, to impose the forcing in (3) to maintain a steady base flow). However, recent Newton-GMRES iteration methods [36] now allow this fully-nonlinear analysis to be performed accurately, as demonstrated by Parker, Caulfield & Kerswell [34] who revealed the unexpected subcritical bifurcation diagram of Kelvin-Helmholtz waves near $J \approx 0.25$ (at $[Re, \theta, Pr, R] = [4000, 0, 1, 1]$, see their § 3.1 and figure 1). Although very costly in computing time, and requiring an extension of the current method to a couple of counter-propagating waves, this course of action appears the most judicious next step.

If the validity and relevance of our (much less costly) weakly-nonlinear analysis is confirmed, two natural extensions would bring its predictions closer to 'real-life' experimental and geophysical flows. First, the extension to three-dimensional perturbations (inhomogeneous in y and z) on a two-dimensional base flow $\mathbf{u}_{00}(y, z)$, as introduced in [12], in order to assess the role of spanwise variations and presence of side-walls, as was done in linear stability in [37]. This is expected to be very tedious (as will be clear from Appendix B and the fact that our streamfunction formulation would no longer hold). Second, a less tedious and probably more rewarding extension to *asymmetric* Holmboe waves, which are commonly found in real flows whenever the velocity and density interface are not exactly coincident as in [5, 12] (*e.g.* if $\rho_{00} = -\tanh R(z - z_0)$ and $z_0 \neq 0$). This extension, and the resulting changes in the stability of fixed points at $|z_0|$ is varied, were conjectured at the end of § III C 5. It would allow progress on the interesting question of nonlinear mode selection, such as predicting the long-time co-existence or sole dominance of either mode, and the dependence on initial conditions (basins of attractions).

Appendix A: Weakly-nonlinear expansions

Below we complement § III with additional information about the hierarchy of nonlinear terms.

1. Single mode: expansion summary

At each successively higher order, new terms are added to the perturbation to match those which were neglected during the calculations at lower order. This results in the hierarchy shown in Table III.

TABLE III: For an single-mode expansion at order m (columns), the crosses denote all wavenumber harmonics n (rows) required (terms $\mathbf{w}_{mn}A^m E^n$). At order $m \geq 2$, the expansion must also include all terms at smaller m (*e.g.* a total of four terms at order 2, six terms at order 3, etc). Although we only considered in this work expansions up to order $m = 3$ (in bold), here we include higher orders for completeness (expanding the Landau equation to obtain a second Landau coefficient would require computation up to order 5).

$m \rightarrow$ $n \downarrow$	0	1	2	3	4	5
0	×		×		×	
1		×		×		×
2			×		×	
3				×		×
4					×	
5						×

2. Double mode: origin of the order 2 and 3 terms

Here we complement the double-mode expansion (21) by explaining the origin of the order 2 terms (table IV) and order 3 terms (table V) from nonlinear interactions, and showing the terms that are implicitly accounted for in the complex conjugate part (+ c.c.). Table V also shows (through its empty cells) the order 3 terms that have been neglected in the expansion (21) because they are not necessary to compute the Landau coefficients.

TABLE IV: Table showing how order 1 terms (left column and top row) multiply to make order 2 terms (main body of the table) in the double-mode analysis. Bold order 2 terms are tracked explicitly in the expansion (21), while non-bold order 2 terms are implicitly accounted for through the complex conjugate.

Order 1 $\downarrow \rightarrow$	A_{110}	A_{101}	A_{1-10}	A_{10-1}
A_{110}	A_{220}	A_{211}	$A_{200}^{(1)}$	A_{21-1}
A_{101}		A_{202}	A_{2-11}	$A_{200}^{(2)}$
A_{1-10}			A_{2-20}	A_{2-1-1}
A_{10-1}				A_{20-2}

TABLE V: Table showing how order 1 terms (left column) and order 2 terms (top row) multiply to make order 3 terms (main body of the table) in the double-mode analysis. Bold and non-bold terms order 3 terms are respectively tracked explicitly and implicitly through the c.c. as in table IV. Empty cells denote order 3 terms that we neglected (20 out of 40, *i.e.* half).

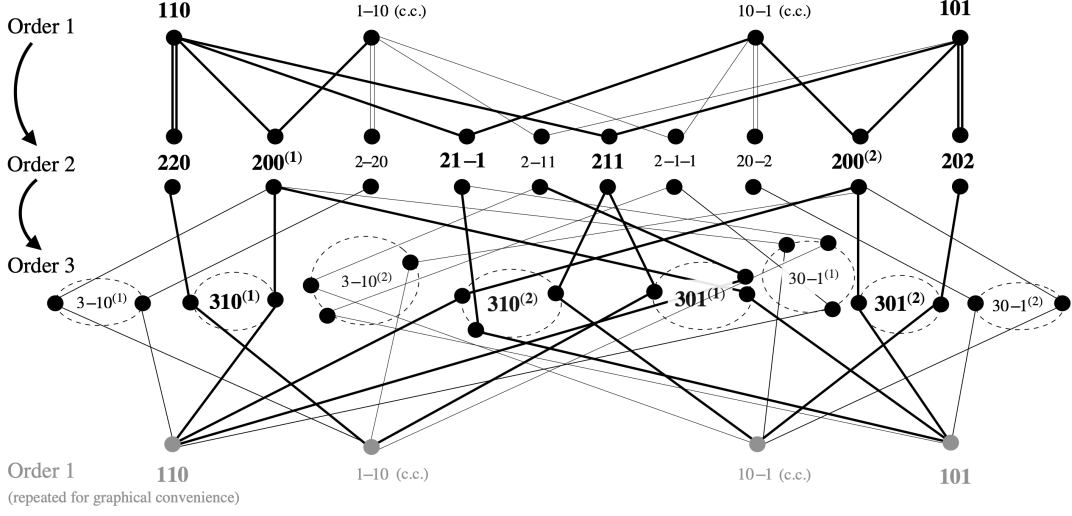| Order 2 $\rightarrow$ Order 1 $\downarrow$	$A_{200}^{(1)}$	$A_{200}^{(2)}$	A_{220}	A_{202}	A_{211}	A_{21-1}	A_{2-20}	A_{20-2}	A_{2-1-1}	A_{2-11}
A_{110}	$A_{310}^{(1)}$	$A_{310}^{(2)}$					$A_{3-10}^{(1)}$		$A_{30-1}^{(1)}$	$A_{301}^{(1)}$
A_{101}	$A_{301}^{(1)}$	$A_{301}^{(2)}$			$A_{310}^{(2)}$			$A_{30-1}^{(2)}$	$A_{3-10}^{(2)}$	
A_{1-10}	$A_{3-10}^{(1)}$	$A_{3-10}^{(2)}$	$A_{310}^{(1)}$		$A_{301}^{(1)}$	$A_{30-1}^{(1)}$				
A_{10-1}	$A_{30-1}^{(1)}$	$A_{30-1}^{(2)}$		$A_{301}^{(2)}$	$A_{310}^{(2)}$					$A_{3-10}^{(2)}$

FIG. 10: Graph representation of tables IV-V. Order 2 terms only have one contribution each, *i.e.* they appear only once in table IV. Each is represented by a bullet representing the product of two order 1 terms. By contrast, order 3 terms have two or three different contributions, *i.e.* as many times as they appear in table IV. Each order 3 term is the sum all the bullets lying on the dashed circle around them, while each bullet represents the product of an order 1 with an order 2 term. As in the tables, bold *vs* non-bold term (and thick *vs* thin lines) are tracked explicitly *vs* implicitly.

Finally, for completeness, we show in figure 10 the information of these tables in graph form. Despite our efforts to adopt a clear notation and our neglect of half the order 3 terms (empty cells in table V), this figure demonstrates that a double-mode expansion at order 3 is already exceedingly challenging to interpret...

Appendix B: Full expressions of the linear operators and forcing terms

1. Single mode

a. Order 1 linear operators

$$\mathscr{A}_k \equiv \begin{bmatrix} -k^2 + \partial_{zz} & 0 \\ 0 & 1 \end{bmatrix} \tag{B1a}$$

$$\mathscr{B}_{(k,\mathbf{Q})} \equiv \begin{bmatrix} -ik\psi'_{00}\left(-k^2 + \partial_{zz}\right) + ik\psi'''_{00} + \dfrac{1}{Re}(k^4 + \partial_{zzzz} - 2k^2\partial_{zz}) & J(\sin\theta\,\partial_z + ik\cos\theta) \\ ik\rho'_{00} & -ik\psi'_{00} + \dfrac{1}{Re\,Pr}\left(-k^2 + \partial_{zz}\right) \end{bmatrix} \tag{B1b}$$

For the next orders, it is convenient to define the linear operator $\mathscr{L}$:

$$\mathscr{L}_{k,\sigma,\mathbf{Q}} \equiv \mathscr{B}_{k,\mathbf{Q}} - \sigma\mathscr{A}_k \equiv \begin{bmatrix} \mathscr{L}_{11} & \mathscr{L}_{12} \\ \mathscr{L}_{21} & \mathscr{L}_{22} \end{bmatrix} \tag{B2}$$

where

$$\mathscr{L}_{11}(k,\sigma,\mathbf{Q}) = -ik\psi'_{00}\left(-k^2 + \partial_{zz}\right) + ik\psi'''_{00} + \frac{1}{Re}(k^4 + \partial_{zzzz} - 2k^2\partial_{zz}) - \sigma(-k^2 + \partial_{zz}) \tag{B3a}$$

$$\mathscr{L}_{12}(k,\sigma,\mathbf{Q}) = J(\sin\theta\,\partial_z + ik\cos\theta) \tag{B3b}$$

$$\mathscr{L}_{21}(k,\sigma,\mathbf{Q}) = ik\rho'_{00} \tag{B3c}$$

$$\mathscr{L}_{22}(k,\sigma,\mathbf{Q}) = -ik\psi'_{00} + \frac{1}{Re\,Pr}\left(-k^2 + \partial_{zz}\right) - \sigma \tag{B3d}$$

b.   Order 2 forcing

$$\mathbf{f}_{20} \equiv \begin{bmatrix} ik\psi_{11}(\psi_{11}^{*'''} - k^2\psi_{11}^{*'}) - ik\psi_{11}^*(\psi_{11}''' - k^2\psi_{11}') \\ -\psi_{11}'(-ik\psi_{11}^{*''} + ik^3\psi_{11}^*) - \psi_{11}^{*'}(ik\psi_{11}'' - ik^3\psi_{11}) \\ ik\psi_{11}'\rho_{11}^* + ik\psi_{11}\rho_{11}^{*'} - ik\psi_{11}^*\rho_{11}' - ik\psi_{11}^{*'}\rho_{11} \end{bmatrix} \tag{B4a}$$

$$\mathbf{f}_{22} \equiv \begin{bmatrix} ik\psi_{11}(\psi_{11}''' - k^2\psi_{11}') - ik\psi_{11}'(\psi_{11}'' - k^2\psi_{11}) \\ ik\psi_{11}\rho_{11}' - ik\psi_{11}'\rho_{11} \end{bmatrix} \tag{B4b}$$

c.   Order 3 forcing

$$\mathbf{f}_{31} \equiv \begin{bmatrix} -2ik\psi_{11}^{*'}(\psi_{22}'' - 4k^2\psi_{22}) - ik\psi_{11}^*(\psi_{22}''' - 4k^2\psi_{22}') + ik\psi_{22}'(\psi_{11}^{*''} - k^2\psi_{11}^*) + \\ 2ik\psi_{22}(\psi_{11}^{*'''} - k^2\psi_{11}^{*'}) - ik\psi_{20}'(\psi_{11}'' - k^2\psi_{11}) + ik\psi_{11}\psi_{20}''' \\ ik\psi_{22}'\rho_{11}^* + 2ik\psi_{22}\rho_{11}^{*'} - 2ik\psi_{11}^{*'}\rho_{22} - ik\psi_{11}^*\rho_{22}' - ik\psi_{20}'\rho_{11} + ik\psi_{11}\rho_{20}' \end{bmatrix} \tag{B5a}$$

$$\mathbf{f}_{33} \equiv \begin{bmatrix} -2ik\psi_{11}'(\psi_{22}'' - 4k^2\psi_{22}) + ik\psi_{11}(\psi_{22}''' - 4k^2\psi_{22}') - \\ ik\psi_{22}'(\psi_{11}'' - k^2\psi_{11}) + 2ik\psi_{22}(\psi_{11}''' - k^2\psi_{11}') \\ -ik\psi_{22}'\rho_{11} + 2ik\psi_{22}\rho_{11}' - 2ik\psi_{11}'\rho_{22} + ik\psi_{11}\rho_{22}' \end{bmatrix} \tag{B5b}$$

2.   Double mode

a.   Order 2 forcing

Mean flow:

$$\mathbf{f}_{200}^{(1)} \equiv \begin{bmatrix} ik\psi_{110}(\psi_{110}^{*'''} - k^2\psi_{110}^{*'}) - ik\psi_{110}^*(\psi_{110}''' - k^2\psi_{110}') \\ -\psi_{110}'(-ik\psi_{110}^{*''} + ik^3\psi_{110}^*) - \psi_{110}^{*'}(ik\psi_{110}'' - ik^3\psi_{110}) \\ ik\psi_{110}'\rho_{110}^* + ik\psi_{110}\rho_{110}^{*'} - ik\psi_{110}^*\rho_{110}' - ik\psi_{110}^{*'}\rho_{110} \end{bmatrix} \tag{B6}$$

Note: $\mathbf{f}_{200}^{(2)}$ is given by replacing the subscripts $_{110}$ by $_{101}$ in (B6).

Second harmonics:

$$\mathbf{f}_{220} \equiv \begin{bmatrix} -ik\psi_{110}'(\psi_{110}' - k^2\psi_{110}) + ik\psi_{110}(\psi_{110}''' - k^2\psi_{110}') \\ ik\psi_{110}'\rho_{110} + ik\psi_{110}\rho_{110}' \end{bmatrix} \tag{B7}$$

Note: $\mathbf{f}_{202}$ is given by replacing the subscripts $_{110}$ by $_{101}$ in (B7).

Breather mode:

$$\mathbf{f}_{21-1} \equiv \begin{bmatrix} ik\psi_{110}'(\psi_{101}^{*''} - k^2\psi_{101}^*) + ik\psi_{110}(\psi_{101}^{*'''} - k^2\psi_{101}^{*'}) \\ -ik\psi_{101}^{*'}(\psi_{110}'' - k^2\psi_{110}) - ik\psi_{101}^*(\psi_{110}''' - k^2\psi_{110}') \\ ik\psi_{110}'\rho_{101}^* + ik\psi_{110}\rho_{101}^{*'} - ik\psi_{101}^*\rho_{110}' - ik\psi_{101}^{*'}\rho_{110} \end{bmatrix} \tag{B8}$$

Mixed mode:

$$\mathbf{f}_{211} \equiv \begin{bmatrix} -ik\psi'_{110}(\psi''_{101} - k^2\psi_{101}) + ik\psi_{110}(\psi'''_{101} - k^2\psi'_{101}) \\ -ik\psi'_{101}(\psi''_{110} - k^2\psi_{110}) + ik\psi_{101}(\psi'''_{110} - k^2\psi'_{110}) \\ \\ -ik\psi'_{110}\rho_{101} + ik\psi_{110}\rho'_{101} - ik\psi'_{101}\rho_{110} + ik\psi_{101}\rho'_{110} \end{bmatrix} \tag{B9}$$

b. Order 3 forcing

$$\mathbf{f}_{310}^{(1)} \equiv \begin{bmatrix} ik\psi_{110}\psi_{200}^{(1)''''} - ik\psi_{200}^{(1)'}(\psi''_{110} - k^2\psi_{110}) - 2ik\psi_{110}^{*'}(\psi''_{220} - 4k^2\psi_{220}) \\ -ik\psi_{110}^*(\psi'''_{220} - 4k^2\psi'_{220}) + ik\psi'_{220}(\psi_{110}^{*''} - k^2\psi_{110}^*) + 2ik\psi_{220}(\psi_{110}^{*'''} - k^2\psi_{110}^{*'}) \\ \\ ik\psi_{110}\rho_{200}^{(1)'} - ik\psi_{200}^{(1)}\rho'_{110} - 2ik\psi_{110}^{*'}\rho_{220} - ik\psi_{110}^*\rho'_{220} + ik\psi'_{220}\rho_{110}^* + 2ik\psi_{220}\rho_{110}^{*'} \end{bmatrix} \tag{B10a}$$

$$\mathbf{f}_{310}^{(2)} \equiv \begin{bmatrix} ik\psi_{101}\psi'''_{21-1} - ik\psi'_{21-1}(\psi''_{101} - k^2\psi_{101}) - 2ik\psi_{101}^{*'}(\psi''_{211} - 4k^2\psi_{211}) \\ -ik\psi_{101}^*(\psi'''_{211} - 4k^2\psi'_{211}) + ik\psi'_{211}(\psi_{101}^{*''} - k^2\psi_{101}^*) \\ +2ik\psi_{211}(\psi_{101}^{*'''} - k^2\psi_{101}^{*'}) + ik\psi_{110}\psi_{200}^{(2)''''} - ik\psi_{200}^{(2)'}(\psi''_{110} - k^2\psi_{110}) \\ \\ ik\psi_{101}\rho'_{21-1} - ik\psi'_{21-1}\rho_{101} - 2ik\psi_{101}^{*'}\rho_{211} - ik\psi_{101}^*\rho'_{211} \\ +ik\psi'_{211}\rho_{101}^* + 2ik\psi_{211}\rho_{101}^{*'} + ik\psi_{110}\rho_{200}^{(2)'} - ik\psi_{200}^{(2)'}\rho_{110} \end{bmatrix} \tag{B10b}$$

$$\mathbf{f}_{301}^{(1)} \equiv \begin{bmatrix} ik\psi_{110}\psi_{21-1}^{*'''} - ik\psi_{21-1}^{*'}(\psi''_{110} - k^2\psi_{110}) - 2ik\psi_{110}^{*'}(\psi''_{211} - 4k^2\psi_{211}) \\ -ik\psi_{110}^*(\psi'''_{211} - 4k^2\psi'_{211}) + ik\psi'_{211}(\psi_{110}^{*''} - k^2\psi_{110}^*) \\ +2ik\psi_{211}(\psi_{110}^{*'''} - k^2\psi_{110}^{*'}) + ik\psi_{101}\psi_{200}^{(1)''''} - ik\psi_{200}^{(1)'}(\psi''_{101} - k^2\psi_{101}) \\ \\ ik\psi_{110}\rho_{21-1}^{*'} - ik\psi_{21-1}^{*'}\rho_{110} - 2ik\psi_{110}^{*'}\rho_{211} - ik\psi_{110}^*\rho'_{211} \\ +ik\psi'_{211}\rho_{110}^* + 2ik\psi_{211}\rho_{110}^{*'} + ik\psi_{101}\rho_{200}^{(1)'} - ik\psi_{200}^{(1)'}\rho_{101} \end{bmatrix} \tag{B10c}$$

$$\mathbf{f}_{301}^{(2)} \equiv \begin{bmatrix} ik\psi_{101}\psi_{200}^{(2)''''} - ik\psi_{200}^{(2)'}(\psi''_{101} - k^2\psi_{101}) - 2ik\psi_{101}^{*'}(\psi''_{202} - 4k^2\psi_{202}) \\ -ik\psi_{101}^*(\psi'''_{202} - 4k^2\psi'_{202}) + ik\psi'_{202}(\psi_{101}^{*''} - k^2\psi_{101}^*) + 2ik\psi_{202}(\psi_{101}^{*'''} - k^2\psi_{101}^{*'}) \\ \\ ik\psi_{101}\rho_{200}^{(2)'} - ik\psi_{200}^{(2)}\rho'_{101} - 2ik\psi_{101}^{*'}\rho_{202} - ik\psi_{101}^*\rho'_{202} + ik\psi'_{202}\rho_{101}^* + 2ik\psi_{202}\rho_{101}^{*'} \end{bmatrix} \tag{B10d}$$

Appendix C: Energy norm matrix $\mathscr{M}$

In our work, the following choice of $\mathscr{M}$ representing total energy was used:

$$\mathscr{M} = \begin{bmatrix} 4\mathbb{D}^H\mathbb{D} + 12k^2\mathbb{I} & 0 \\ 0 & J \cdot \mathbb{I} \end{bmatrix}, \tag{C1}$$

where $\mathbb{I}$ is the identity matrix and $\mathbb{D}$ the discretized first order differentiation operator.

This corresponds to a discretized action of the bilinear form:

$$\langle[\psi_1, \rho_1], [\psi_2, \rho_2]\rangle_{\mathscr{M}} \longmapsto 4\Re(\partial_z\psi_1)\Re(\partial_z\psi_2) + 4\Re(\partial_x\psi_1)\Re(\partial_x\psi_2) + 4J\Re(\rho_1)\Re(\rho_2), \tag{C2}$$

on $\mathbf{w}_{11}, \mathbf{w}_{31}$ (see (17)). This form was chosen such that the norm of a state vector $[\psi(x,z), \rho(x,z)] = [\hat{\psi}(z)e^{ikx}, \hat{\rho}(z)e^{ikx}] +$ c.c. at $x = 0$ is given by:

$$\langle\mathbf{w}, \mathbf{w}\rangle_{\mathscr{M}} = \langle[\psi, \rho], [\psi, \rho]\rangle_{\mathscr{M}}|_{x=0} = \left\{2\Re(\partial_z\hat{\psi})\right\}^2 + \left\{2\Re(ik\hat{\psi})\right\}^2 + J\left\{2\Re(\hat{\rho})\right\}^2$$
$$= \sum_z u^2(0, z) + w^2(0, z) + J\rho^2(0, z) \tag{C3}$$

which is twice the sum of the kinetic and scalar energies, as desired (the scalar variance ρ^2 contributes in proportion to the stratification J).

Appendix D: Solvability condition

This solvability condition (or Fredholm alternative) method to solve for the Landau coefficient K was never used in our work because the method of [25] described in § III B 4 and (16) was sufficient. It is included here for completeness and in case future extensions of this work suffer from poor conditioning of $\hat{\mathscr{L}}_{(k,\sigma+2\sigma_r,\mathbf{Q})}$ as $\mathbf{Q} \to \mathbf{Q}_c, \sigma_r \to 0$, and thus require this method.

To enforce the solvability condition, we consider the adjoint problem of (9) (which we recall is $\mathscr{L}_{k,\sigma,\mathbf{Q}} \mathbf{w}_{11} = 0$), defined formally as:

$$\mathscr{L}_{k,\sigma,\mathbf{Q}}^{\dagger} \mathbf{w}_{11}^{\dagger} = 0, \tag{D1}$$

where $\mathscr{L}_{k,\sigma,\mathbf{Q}}^{\dagger}$ is the adjoint operator and $\mathbf{w}_{11}^{\dagger}$ the adjoint eigenvector. Since the numerical discretization and adjoint operators do not necessarily commute, care must be exercised in computing the actual discretized adjoint operator. A simple practical way to do so is to remove boundary conditions on the discretized direct operator, take its complex conjugate transpose (^{H}), before finally adding adjoint boundary conditions.

We now take the inner product of $\mathbf{w}_{11}^{\dagger}$ with (16) in the limit $\sigma_r \to 0$:

$$\langle \mathbf{w}_{11}^{\dagger}, \mathscr{L}_{k,\sigma,\mathbf{Q}} \mathbf{w}_{31} \rangle = K \langle \mathbf{w}_{11}^{\dagger}, \mathscr{A}_k \mathbf{w}_{11} \rangle + \langle \mathbf{w}_{11}^{\dagger}, \mathbf{f}_{31} \rangle \quad \text{(by (16))}$$

$$\implies \underbrace{\langle \mathscr{L}_{k,\sigma,\mathbf{Q}}^{\dagger} \mathbf{w}_{11}^{\dagger}, \mathbf{w}_{31} \rangle}_{=0} = K \langle \mathbf{w}_{11}^{\dagger}, \mathscr{A}_k \mathbf{w}_{11} \rangle + \langle \mathbf{w}_{11}^{\dagger}, \mathbf{f}_{31} \rangle \quad \text{(by (D1))} \tag{D2}$$

$$\implies K = -\frac{\langle \mathbf{w}_{11}^{\dagger}, \mathbf{f}_{31} \rangle}{\langle \mathbf{w}_{11}^{\dagger}, \mathscr{A}_k \mathbf{w}_{11} \rangle}, \tag{D3}$$

assuming that $\langle \mathbf{w}_{11}^{\dagger}, \mathscr{A}_k \mathbf{w}_{11} \rangle \neq 0$. We recall that $\mathscr{A}_k$ is given in (9), and that the inner product is with respect to $\mathscr{M}$ as in (17), (C1).

It is worth noting that in the limit $\mathbf{Q} \to \mathbf{Q}_C$, $K = \langle \mathbf{w}_{11}^{\dagger}, \mathbf{f}_{31} \rangle$ is independent of $\mathscr{M}$ (consistent with the fact that K is always uniquely defined in the case $\sigma_r \to 0$).

BIBLIOGRAPHY

[1] H. Salehipour, C. P. Caulfield, and W. R. Peltier, "Turbulent mixing due to the Holmboe wave instability at high Reynolds number," *Journal of Fluid Mechanics*, vol. 803, pp. 591–621, Sept. 2016.

[2] W. D. Smyth, G. P. Klaassen, and W. R. Peltier, "Finite amplitude Holmboe waves," *Geophysical & Astrophysical Fluid Dynamics*, vol. 43, pp. 181–222, Dec. 1988.

[3] W. D. Smyth and W. R. Peltier, "Instability and transition in finite-amplitude Kelvin–Helmholtz and Holmboe waves," *Journal of Fluid Mechanics*, vol. 228, pp. 387–415, 1991.

[4] W. D. Smyth, J. R. Carpenter, and G. A. Lawrence, "Mixing in symmetric Holmboe waves," *Journal of Physical Oceanography*, vol. 37, pp. 1566–1583, June 2007.

[5] J. R. Carpenter, G. A. Lawrence, and W. D. Smyth, "Evolution and mixing of asymmetric Holmboe instabilities," *Journal of Fluid Mechanics*, vol. 582, pp. 103–132, July 2007.

[6] J. R. Carpenter, E. W. Tedford, M. Rahmani, and G. A. Lawrence, "Holmboe wave fields in simulation and experiment," *Journal of Fluid Mechanics*, vol. 648, pp. 205–223, Apr. 2010.

[7] K. M. Smith, C. P. Caulfield, and J. R. Taylor, "Turbulence in forced stratified exchange flows," *Submitted*, 2020.

[8] E. O. Macagno and H. Rouse, "Interfacial mixing in stratified flow," *Journal of the Engineering Mechanics Division. Proceeding of the American Society of Civil Engineers*, vol. 87, no. EM5, pp. 55–81, 1961.

[9] E. W. Tedford, R. Pieters, and G. A. Lawrence, "Symmetric Holmboe instabilities in a laboratory exchange flow," *Journal of Fluid Mechanics*, vol. 636, p. 137, Oct. 2009.

[10] C. R. Meyer and P. F. Linden, "Stratified shear flow: experiments in an inclined duct," *Journal of Fluid Mechanics*, vol. 753, pp. 242–253, Aug. 2014.

[11] A. Lefauve, *Waves and turbulence in sustained stratified shear flows*. PhD thesis, University of Cambridge. doi:10.17863/CAM.24648, 2018.

[12] A. Lefauve, J. L. Partridge, Q. Zhou, C. P. Caulfield, S. B. Dalziel, and P. F. Linden, "The structure and origin of confined Holmboe waves," *Journal of Fluid Mechanics*, vol. 848, pp. 508–544, 2018.

[13] J.-M. Chomaz, "A flow on the verge of turbulent breakdown," *Journal of Fluid Mechanics*, vol. 854, pp. 1–4, 2018.

[14] J. T. Stuart, "On the non-linear mechanics of hydrodynamic stability," *Journal of Fluid Mechanics*, vol. 4, pp. 1–21, 1958.

[15] J. T. Stuart, "On the non-linear mechanisms of wave disturbances in stable and unstable parallel flows. Part 1. the basic behaviour in plane Poiseuille flow," *Journal of Fluid Mechanics*, vol. 9, pp. 353–370, 1960.

[16] J. Watson, "On the non-linear mechanisms of wave disturbances in stable and unstable parallel flows. Part 2. the development of a solution for plane Poiseuille flow and for plane Couette flow," *Journal of Fluid Mechanics*, vol. 9, pp. 371–389, 1960.

[17] S. A. Maslowe, "Weakly nonlinear stability of a viscous free shear-layer," *Journal of Fluid Mechanics*, vol. 79, pp. 689–702, 1977.

[18] S. M. Churilov and I. G. Shukhman, "Nonlinear stability of a stratified shear flow: a viscous critical layer," *Journal of Fluid Mechanics*, vol. 180, pp. 1–20, 1987.

[19] A. Davey and H. P. F. Nguyen, "Finite-amplitude stability of pipe flow," *Journal of Fluid Mechanics*, vol. 45, pp. 701 – 720, 1971.

[20] N. Itoh, "Nonlinear stability of parallel flows with subcritical reynolds-numbers. part 2. stability of pipe poiseuille flow to finite axisymmetric disturbances," *Journal of Fluid Mechanics*, vol. 82, pp. 469–479, 1977.

[21] S. A. Maslowe, "Weakly nonlinear stability theory of stratified shear flows," *Quaterly Journal of the Royal Meteorological Society*, vol. 103, pp. 769–783, 1977.

[22] S. N. Brown, A. S. Rosen, and S. A. Maslowe, "The evolution of a quasi-steady critical layer in a stratified viscous shear layer," *Proc. R. Soc. Lond. A*, vol. 375, no. 1761, pp. 167–186, 1981.

[23] T. Herbert, "On perturbation methods in nonlinear stability theory," *Journal of Fluid Mechanics*, vol. 126, pp. 167–186, 1983.

[24] K. Fujimura, "The equivalence between two perturbation methods in weakly nonlinear stability theory for parallel shear flows," *Proc. R. Soc. Lond.*, vol. 424, pp. 373–392, 1989.

[25] K. G. Pham and S. A. Suslov, "On the definition of Landau constants in amplitude equations away from a critical point," *Royal Society Open Science*, vol. 5, p. 180746, 2018.

[26] P. Dey and S. A. Suslov, "Nonlinear interaction of thermogravitational waves and thermomagnetic rolls in a vertical layer of ferrofluid placed in a normal magnetic field," *Physics of Fluids*, vol. 31, p. 014105, 2019.

[27] P. Hazel, "Numerical studies of the stability of inviscid stratified shear flows," *Journal of Fluid Mechanics*, vol. 51, no. 01, pp. 39–61, 1972.

[28] G. A. Lawrence, F. K. Browand, and L. G. Redekopp, "The stability of a sheared density interface," *Physics of Fluids A: Fluid Dynamics*, vol. 3, no. 10, pp. 2360–2370, 1991.

[29] W. D. Smyth and J. R. Carpenter, *Instability in Geophysical Flows*. Cambridge University Press, 2019.

[30] C. J. Howland, J. R. Taylor, and C. P. Caulfield, "Testing linear marginal stability in stratified shear layers," *Journal of Fluid Mechanics*, vol. 839, p. R4, 2018.

[31] S. A. Suslov, "Two-equation model of mean flow resonances in subcritical flow systems," *Discret. Cont. Dyn.*, vol. S.-S 1, p. 165 – 176, 2008.

[32] J. L. Partridge, A. Lefauve, and S. B. Dalziel, "A versatile scanning method for volumetric measurements of velocity and density fields," *Measurement Science and Technology*, vol. 30, p. 055203, 2019.

[33] V. Mantič-Lugo, C. Arratia, and F. Gallaire, "Self-consistent mean flow description of the nonlinear saturation of the vortex shedding in the cylinder wake," *Physical Review Letters*, vol. 113, p. 084501, 2014.

[34] J. P. Parker, C. P. Caulfield, and R. R. Kerswell, "Kelvin–Helmholtz billows above Richardson number 1/4," *Journal of Fluid Mechanics*, vol. 879, p. R1, 2019.

[35] S. Pasche, F. Avellan, and F. Gallaire, "Vortex streamwise impingement onto an axisymmetric obstacle: Subcritical vortex breakdown," *Submitted*, 2020.

[36] G. J. Chandler and R. R. Kerswell, "Invariant recurrent solutions embedded in a turbulent two-dimensional Kolmogorov flow," *Journal of Fluid Mechanics*, vol. 722, pp. 554–595, May 2013.

[37] Y.-M. Ducimetière, F. Gallaire, A. Lefauve, and C. P. Caulfield, "The effects of spanwise confinement on stratified shear instabilities," *In preparation*, 2021.